J. Fluid Mech. (2002), *vol.* 457, *pp.* 1–34.
DOI: 10.1017/S0022112001007613 Printed in the United Kingdom

Drag reduction in wall-bounded turbulence via a transverse travelling wave

By YIQING DU, V. SYMEONIDIS AND G. E. KARNIADAKIS†

Division of Applied Mathematics, Brown University, Providence, RI 02912, USA

(Received 29 May 2000 and in revised form 20 September 2001)

Computational experiments based on direct numerical simulation of wall-bounded flow reveal that turbulence production can be suppressed by the action of a transverse travelling wave. Flow visualizations show that the near-wall flow structure is altered substantially, compared to other turbulence control techniques, leading to a large amount of shear stress reduction (i.e., more than 30%). The travelling wave can be induced by a spanwise force that is confined within the viscous sublayer, it has its maximum at the wall, and decays exponentially away from it. We demonstrate the robustness of this approach, and its application in salt water using arrays of electro-magnetic tiles that can produce the required travelling wave excitation. We also study corresponding results from spanwise oscillations using a similar force, which also leads to large drag reduction. Although the turbulence statistics for the two approaches are similar, the near-wall structures appear to be different: in the spanwise oscillatory excitation there is a clear presence of wall-streaks whereas in the travelling wave excitation these streaks have disappeared. From the fundamental point of view, the new finding of this work is that appropriate enhancement of the streamwise vortices leads to weakening of the streak intensity, as measured by the normal vorticity component, and correspondingly substantial suppression of turbulence production. From the practical point of view, our findings provide guidance for designing different surface-based actuation techniques including piezoelectric materials, shape memory alloys, and electro-magnetic tiles.

1. Introduction

Direct evidence linking the organized vortical structure of turbulent boundary layers and measurable stress quantities in the flow has been provided in many numerical simulation studies (e.g. Bernard, Thomas & Handler 1993; Kravchenko, Choi & Moin 1993; and Jimenez & Pinelli 1999). In Bernard *et al.* (1993), analysis of numerical data for turbulent flow in a channel demonstrated that Reynolds stress production is linked directly to the dynamics of quasi-streamwise vortical structures in the wall region. In Kravchenko *et al.* (1993), streamwise vortices were generally observed to lie directly above and displaced laterally from high-skin-friction regions. Also, the net drag associated with regions of strong streamwise vortices was larger than the mean skin friction for the entire wall. In Jimenez & Pinelli (1999) the turbulence regeneration cycle was shown to be associated with the near-wall region only and independent of the outer flow. Interrupting the streak cycle artificially led to large

† Author to whom correspondence should be addressed: gk@cfm.brown.edu

drag reduction and even flow re-laminarization. Based on this and other experimental evidence (e.g. Swearingen & Blackwelder 1987), the focus in modern drag reduction techniques has been on controlling locally individual streamwise vortices based on sophisticated but often rather complex closed-loop control strategies (Lee *et al.* 1997; Rathnasingham & Breuer 1997). While effective, such approaches may be inefficient or not even feasible in the high Reynolds number regime where length scales are of the order of tens of microns.

The guiding fundamental principle behind such approaches has been the weakening of streamwise vortices and the simultaneous enhancement of spanwise vorticity. This theme has been followed in many turbulence control strategies (see Gad-el-Hak 2000). For example, oscillating the wall along the spanwise direction in a turbulent boundary layer flow leads to large drag reduction of more than 30% as was found numerically by Jung, Mangiavacchi & Akhavan (1992) and experimentally by Choi, DeBisschop & Clayton (1998). The basic mechanism of drag reduction in this case has been attributed to the weakening of the intensity of *streamwise vorticity* fluctuations by almost a factor of two across the entire thickness of the boundary layer (see DNS studies of Baron & Quadrio 1996). On the other hand, it has been reported that a net *spanwise vorticity* was created in the boundary layer during the upward as well as downward motion of the oscillating wall (see Choi 2001).

Consistent with this practice is the view (Swearingen & Blackwelder 1987) that the instability of low-speed wall streaks is responsible for sustaining the turbulence cycle, and more recent theories by Jimenez & Pinelli (1999), Schoppa & Hussain (1997) and Waleffe (1997) have provided fundamental insight into this process. In particular, Schoppa & Hussain (1998), capitalizing on their result, proposed a promising turbulent drag reduction strategy based on a model of streamwise generators centred at the edge of the boundary layer (channel centreline in their DNS study). The interesting aspect of this approach is that it introduces substantial streamwise vorticity, it is a large-scale excitation, and it leads to large (more than 20%) drag reduction at a relatively small excitation amplitude. Despite the introduction of external vorticity along the flow direction, the normal vorticity fluctuations of the controlled field were suppressed by a factor of about two compared to the uncontrolled case.

In an independent experimental investigation, Nosenchuck & Brown (1993) and Nosenchuck (1996), also motivated by the same principle of weakening the streamwise vorticity, designed an array of electro-magnetic (EM) tiles to suppress turbulence of weakly conductive fluids. Specifically, they claimed that streamwise vorticity can be substantially reduced if electrodes with different polarity are activated sequentially in a multi-phase pattern, thus producing locally sources of vorticity with opposite sign to the incoming flow vorticity. In addition, it was argued that a predominantly spanwise source of vorticity is introduced as a result of the $\nabla \times \boldsymbol{F}_l$, where $\boldsymbol{F}_l$ is the induced Lorentz force. Large amounts of drag reduction were reported by Nosenchuck and collaborators but extensive numerical simulations of these designs by Crawford (1996) and Du (1999) as well as simulations by O'Sullivan & Biringen (1998) for a similar design by Bandyopadhyay & Castano (1996) did not show any significant drag reduction.

In the current work, we study the interactions caused by a new way of introducing streamwise vorticity into a turbulent boundary layer. Specifically, we consider a spanwise excitation in the form of a travelling wave, which is confined within the viscous sublayer. The induced streamwise vorticity has also a travelling wave form. This excitation is different from the Lorentz force excitation produced in Nosenchuck's electro-magnetic tiles. In fact, travelling waves have also been seen in those exper-

iments for a multi-phase excitation pattern. This configuration is also studied here and the presence of travelling waves is confirmed. However, the flow visualizations in the experiments reveal waves propagating at an oblique direction, presumably driven by both the spanwise and streamwise components of the Lorentz force. It is shown in the present paper (see Du 1999 for details) that indeed the streamwise component is of magnitude comparable to the spanwise component of the Lorentz force. Previous experimental (Henoch & Stace 1995) as well as numerical investigation (Crawford & Karniadakis 1997) have shown that streamwise Lorentz force excitation leads to net drag increase and enhancement of turbulence intensity.

The transverse Lorentz force excitation studied here leads to suppression of turbulence production and corresponding drag reduction of more than 30%, for travelling waves of appropriate frequency, wavelength and effective penetration of the force into the fluid. The required wavelength, in particular, spans across many pairs of wall streaks, and this makes the proposed method both feasible and efficient. Another important aspect of this new control is that the wall streaks are partially stabilized and in many cases most of them are eliminated. Typically, in other drag reduction techniques the wall streak spacing may increase or the streaks may appear more organized but the familiar picture of pairs of high- and low-speed streaks is not altered. We also study and contrast the travelling wave excitation with an oscillatory force excitation, which can be produced by electro-magnetic strips oriented along the spanwise direction. This form of excitation is similar to spanwise wall oscillations, and leads to substantial net drag reduction. However, in this case too the fundamental near-wall structure of turbulence remains basically unaltered.

In the following, we first describe the simulation of the multi-phase electro-magnetic control in § 2. In § 3, we present results from the oscillatory excitation, and in § 4 we present results from the travelling wave excitation. Preliminary results related to § 4 were first reported in Du & Karniadakis (2000); here we demonstrate the robustness of the proposed excitation by exploring the parameter space and employing non-ideal travelling waveforms. In addition, we provide details of the flow structures for representative cases. We conclude in § 5 with a summary and a brief discussion on the feasibility and efficiency of the new control method. Validation results are included in the Appendix.

2. Results from EM turbulence control – EMTC

We first review some results obtained from a DNS of a companion experiment conducted at Princeton University by Nosenchuck and collaborators using electro-magnetic turbulence control (EMTC) based on an array of tiles (Nosenchuck & Brown 1993; also, Nosenchuck private communications). A single electro-magnetic tile unit consisting of two electrodes and two magnets perpendicular to the flow is shown in figure 1. The magnetic field is 0.5 T and the the electric field is $100\,\mathrm{V\,m^{-1}}$. This unit is repeated periodically to cover the controlled region of a flat plate. The produced Lorentz force is three-dimensional with the largest component in the normal direction. The spanwise force has about the same magnitude (although smaller), while the streamwise component is one-third of the spanwise one (Crawford 1996; Du 1999). Of particular interest is the form of excitation, i.e. the pulsing strategy, which is accomplished via an elaborate 16-phase scheme, with non-dimensional frequency of 3.5 between each excitation cycle (the non-dimensional frequency is based on the convective time scale, which, in turn, is defined by the half-channel width and the centreline velocity).

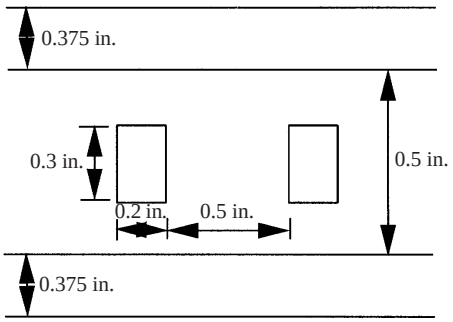

FIGURE 1. Plan view and dimensions of a single electro-magnetic tile used in the Princeton experiment. The two permanent magnets are denoted by the horizontal lines (0.5 in. apart) and the two electrodes by the rectangles. The entire pattern is produced by repeating this unit many times along the streamwise (vertical) and spanwise (horizontal) directions. The flow is perpendicular to the magnets.

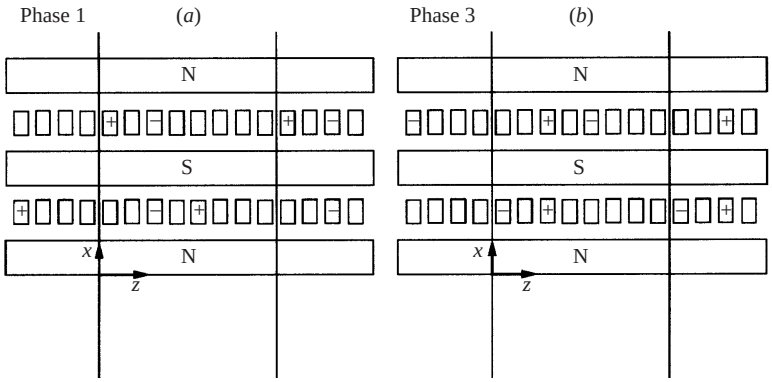

FIGURE 2. (*a*) Pattern of the first phase in Class I; (*b*) pattern of the first phase in Class II. N and S refer to a magnet with North and South polarity, respectively. Phase 1 and Phase 3 on the plot refer to the global phase numbering 1 to 16. The flow is perpendicular to the magnets.

Specifically, the 16 phases can be classified into two categories, each having eight phases. We refer to them as 'Class I' and 'Class II' phases. In the first class, all negative electrodes are aligned in the streamwise x-direction. In the second class, all positive electrodes are aligned in the streamwise x-direction. The first phase of Class I is shown in the plot of figure 2(*a*). Here '+' denotes positively activated electrodes and '−' denotes negatively activated electrodes. Each subsequent phase in this class shifts the entire pattern one electrode over in the positive spanwise z-direction. The first phase in Class II is also shown in figure 2(*b*). Again, each subsequent phase in this class shifts the entire pattern one electrode over in the positive spanwise z-direction. The 16-phase pulsing pattern is formed by taking two consecutive phases in each class alternately. First, we take the first two phases in Class I (i.e. 1 and 2), followed by the first two phases in Class II (3 and 4); then, we take the next two phases in Class I, and so on.

In the simulations, a channel is used as computational domain with only the lower wall subject to electro-magnetic control. The Reynolds number based on the channel half-width and the wall shear velocity of the uncontrolled flow is $Re_\tau \approx 150$. More details on the simulation and validation with a specially designed single-tile experiment are presented in the Appendices (see also Du 1999). In figure 3(*a*), we plot the time history of streamwise vorticity and its corresponding spectrum at a

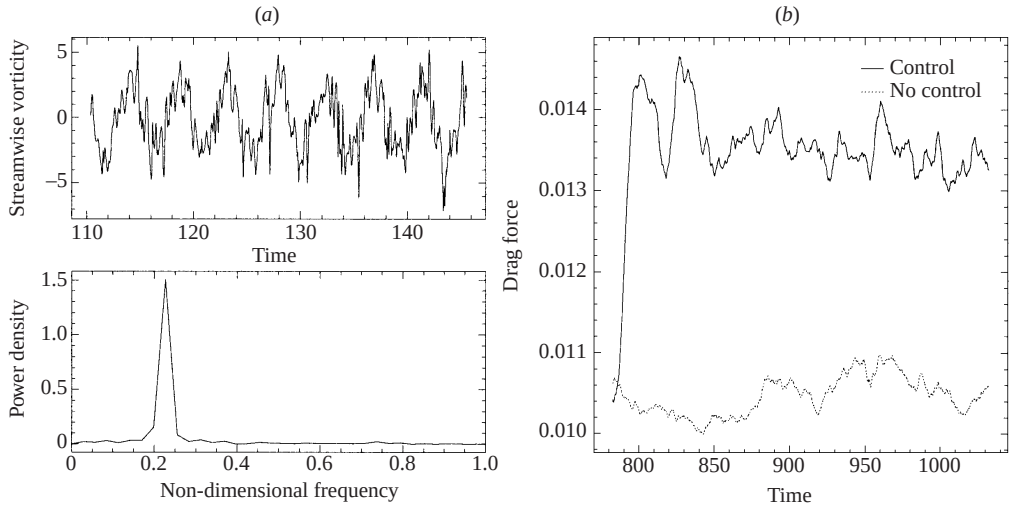

FIGURE 3. (*a*) Time history and corresponding spectrum of streamwise vorticity taken at a point close to the wall; (*b*) time history of drag force on the controlled and no-controlled walls. The values of vorticity, frequency, drag force and time are all in non-dimensional global units.

point above the centre of one tile unit between two electrodes and very close to the wall ($y^+ \approx 2$). There is a peak at non-dimensional frequency 0.22 (convective time units), which is exactly the frequency of the 16-phase imposed pulsing pattern (in convective time units $3.5/16 \approx 0.22$). The time history of the total drag force is shown in figure 3(*b*) for both the controlled and no-control walls. For smaller voltage values employed in the experiment and the simulation a slight increase in drag was observed but for larger values a drag increase by more than 30% is obtained as shown in the figure. This finding is consistent with experiments performed at the Naval Undersea Warfare Center (NUWC) (R. Philips, private communications). This overall increase in drag force is also consistent with an increase in all three velocity turbulence intensities as shown in figure 4. The large value of the spanwise velocity fluctuation is related to the coherent spanwise motion induced by this type of electro-magnetic control. In the following, we examine in more detail corresponding flow patterns.

2.1. *Near-wall flow structure: spanwise oscillations or travelling waves?*

In order to better understand the effect of EMTC we examined systematically the flow field with focus on the near-wall structures. By following many frames of the flow per cycle we were able to detect a coherent spanwise-periodic motion. In figure 5, we present contours of spanwise velocity on a plane close to the wall ($y^+ \approx 3$) at the end of phases 1, 5, 9 and 13. Rectangles denote the electrodes: more specifically black rectangles are negatively activated whereas white (or blank) rectangles are positively activated. The rest of the electrodes are non-active at that time instant. The red colours denote flow in the positive spanwise direction, and blue colours flow in the negative spanwise direction. The penetration of the Lorentz force excitation into the fluid is quantified in figure 6; it shows profiles of the spanwise velocity along the vertical direction. We observe that the induced velocity is substantial within the first five (viscous) units from the wall. From the flow visualizations and these velocity profiles, we can see that strips of fluid along the streamwise direction are being 'propelled' along the spanwise direction in a periodic fashion, resembling

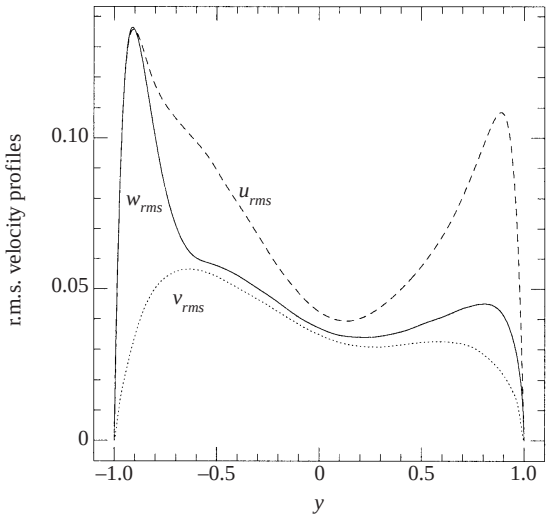

FIGURE 4. Profiles of turbulence intensities for the three velocity components (global units). The controlled wall is at $y = -1$ and the no-control wall at $y = 1$ (also in global units).

either transverse *travelling waves* or *oscillations*. We examine the effect of each such excitation separately in the next two sections.

3. Transverse oscillatory excitation

A uni-directional Lorentz force can be produced by arranging magnets and electrodes in an alternating fashion (Tsinober 1990). This configuration aligned with the flow direction was employed in both experimental (Henoch & Stace 1995) as well as numerical studies (Crawford & Karniadakis 1997) to investigate the possibility of drag reduction in wall-bounded turbulence, but this approach was proved ineffective. However, substantial drag reduction is obtained if a similar excitation is applied along the *spanwise direction* forcing the flow to oscillate at a certain frequency, as we show below (see also Berger *et al.* 2000 for a detailed study).

To simplify matters, we approximate the spanwise Lorentz force by

$$F_z = I\mathrm{e}^{-y/\Delta}\sin(\omega t), \tag{3.1}$$

where $I = 1$ is the (non-dimensional) amplitude of excitation or *interaction parameter*, which is proportional to the product of the magnetic and electric fields, and $\omega = 2\pi/T$ with T the period of the oscillation. Also, $\Delta^+ = 3$ (in viscous units) is the effective penetration of the Lorentz force. It is defined directly by equation (3.1), and its value is determined by the size of the electrodes (see Du, Crawford & Karniadakis 1998 for a detailed discussion). The upper wall is practically unaffected by the Lorentz force applied at the lower wall due to the fast decay of the Lorentz force. That is, the mean and turbulent intensities do not depend on the upper wall although the higher-order statistics (i.e. skewness and flatness) may be affected. However, the amount of drag reduction is not affected by the presence of the upper wall.

In the simulation, we can compare simultaneously and under identical conditions the uncontrolled and the controlled walls. Equation (3.1) assumes that both the electric and magnetic fields are sinusoidal. This is only approximately true for finite size of electrodes and magnets. This effect can also be taken into account, and closed-form

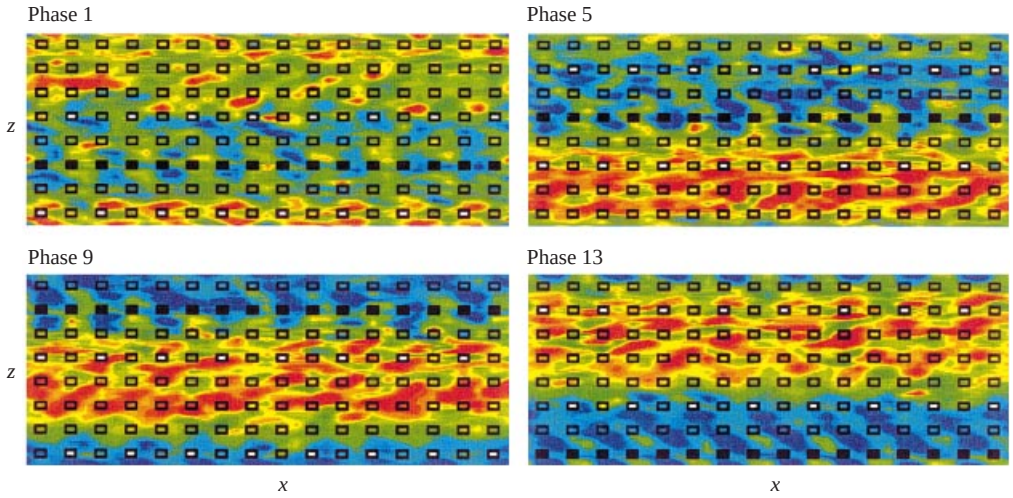

FIGURE 5. Contours of spanwise velocity ($y^+ = 3$) taken at the end of different phases of the excitation cycle as indicated. A periodic spanwise motion is induced by the electro-magnetic pulsing. The rectangles denote the location of electrodes, with black rectangles denoting negative charge and white rectangles positive.

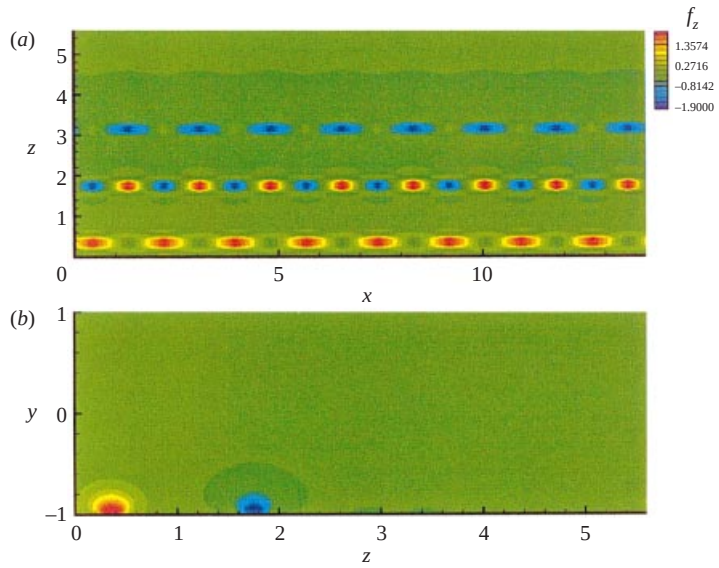

FIGURE 16. Contours of instantaneous spanwise Lorentz force generated during one phase in the 16-phase Princeton multi-tile configuration. (*a*) Plan view; (*b*) cross-flow view.

solutions in the form of series expansions have been derived in Du (1999); they include relatively small correction terms. These more accurate solutions also verify the exponential decay of the Lorentz force.

We have run simulations with three oscillatory excitations corresponding to $T^+ =$ 50, 100 and 200, where $T^+ = Tu_\tau^2/\nu$. The Reynolds number is $Re_\tau \approx 150$ defined as in the previous section. Figure 7 shows a typical time history of the total drag force on the lower (control) wall ($y = -1$) and upper wall ($y = 1$) for the case with

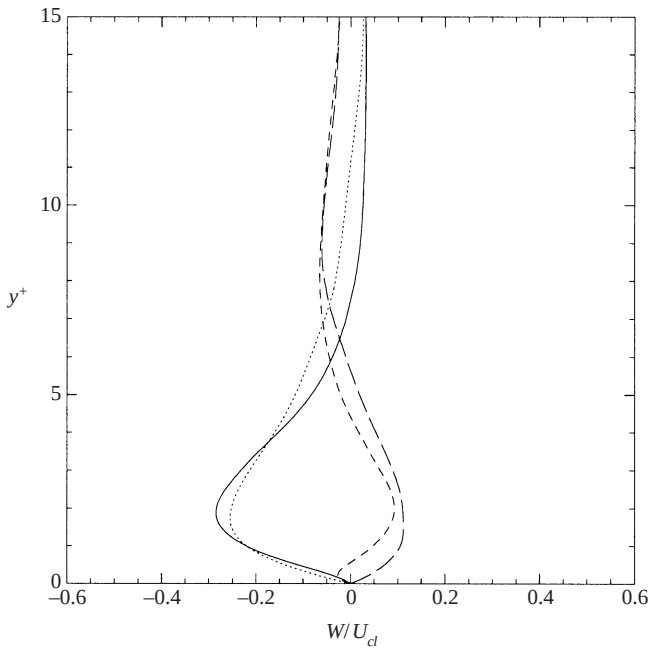

FIGURE 6. Vertical profiles of spanwise velocity (normalized with the centreline streamwise velocity) taken at different times. Here $y^+ = 0$ corresponds to the surface of the controlled wall.

$T^+ = 100$. This case results in the biggest drag reduction reaching more than 35% asymptotically. Similarly, the case corresponding to $T^+ = 50$ leads to drag reduction close to 30% but the case with $T^+ = 200$ results in drag increase. These amounts depend on the penetration length Δ and the Reynolds number Re_τ; a systematic study of those effects was carried out in Berger *et al.* (2000).

In figure 8 we plot the velocity and vorticity turbulence intensities for the case corresponding to largest drag reduction, i.e. $T^+ = 100$. The r.m.s. levels are reduced for the streamwise and normal velocity components at the controlled wall for the drag reducing case but they all increase for the drag increasing case (see Du 1999). The large r.m.s. values of the spanwise component are associated with the oscillatory motion induced by the Lorentz force.

3.1. *Interference with the Stokes layer*

The results obtained with the oscillatory Lorentz force are consistent with the oscillating wall results of Jung *et al.* (1992), which show that at frequency corresponding to $T^+ \approx 110$ the largest amount of drag reduction is achieved. In particular, a physical argument was presented by Jung *et al.* (1992) on the selection of the optimum oscillating frequency. It is based on the hypothesis that the edge of the Stokes layer generated by the oscillating wall is about 2.5 in terms of the non-dimensional units $y^* = y\sqrt{\omega/2\nu}$ above the wall. The location of the centre of near-wall streamwise vortices is about 15 in wall units $y^+ = yu_\tau/\nu$. If we match these two length scales, we obtain a value of $T^+ \approx 110$:

$$\frac{2.5\sqrt{(2\nu/\omega)}u_\tau}{\nu} \approx 15$$

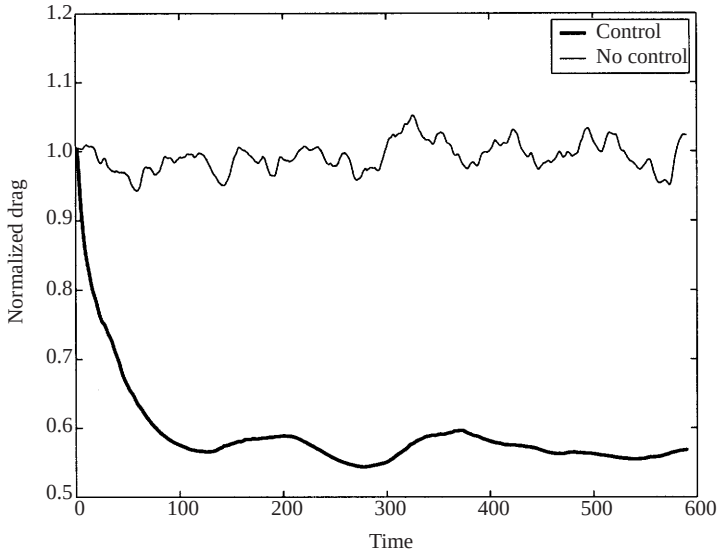

FIGURE 7. Time histories of drag forces on the lower (controlled) wall and upper (no-control) wall for simulations with $I = 1$, $T^+ = 100$. All forces are normalized with the initial no-control value at $t = 0$. Time is non-dimensional in convective units.

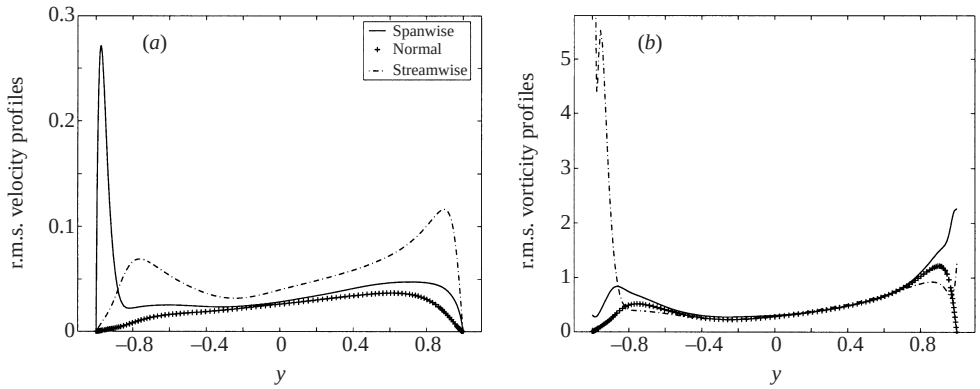

FIGURE 8. Velocity (a) and vorticity (b) turbulence intensities for all components corresponding to a drag reducing case $T^+ = 100$.

which corresponds to

$$T^+ \approx 110.$$

It was then argued that at the frequency corresponding to this period, the Stokes layer generated by the oscillating wall interferes with the turbulence production cycle by suppressing the bursting and sweeping events to the greatest extent, and hence maximum drag reduction is achieved at such excitation conditions. In figure 9, we plot profiles of spanwise velocity normalized by the centreline streamwise velocity for the case $T^+ = 100$. We can see that a Stokes layer with thickness $y^* = 2.5$ is also generated similar to the excitation by the oscillating wall. Experimental results

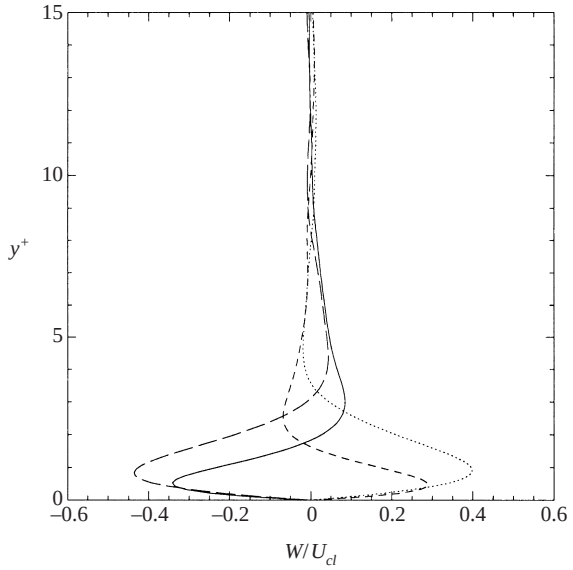

FIGURE 9. Spanwise velocity profiles for the spanwise oscillatory excitation taken at different time instances. They are normalized with the centreline streamwise velocity.

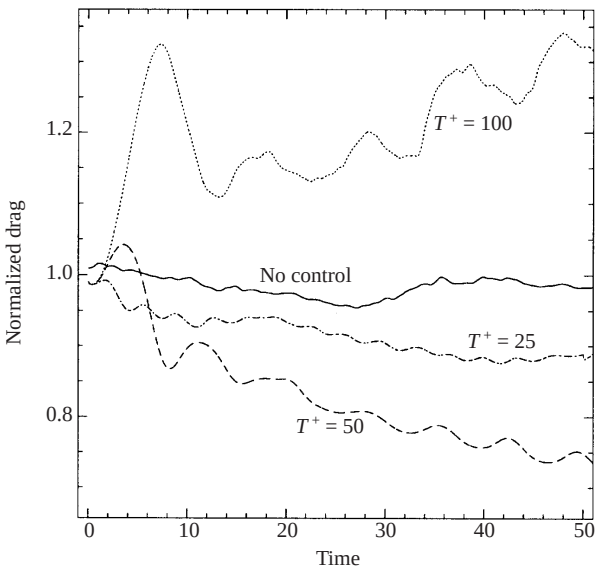

FIGURE 10. Effect of frequency: time history of normalized drag force for $\lambda_z = 5.6$, $I = 1$, $\Delta^+ = 3$ and $T^+ = 100, 50, 25$.

by Choi *et al.* (1998) have verified and extended the results of Jung *et al.* (1992). However, a different physical scenario has been postulated by Choi (2001) based on the change of sign of streamwise vorticity during the oscillation caused by the induced vortex sheet close to the wall. We will return to this point later in § 4.7.

4. Transverse travelling wave excitation

An excitation that would induce spanwise motions closer to the ones observed in the simulation of the Princeton multi-tile configuration (see § 2) is that of a Lorentz force resembling a travelling wave along the span as follows:

$$F_z = I\,\mathrm{e}^{-y/\Delta}\sin\left(\frac{2\pi}{\lambda_z}z - \frac{2\pi}{T}t\right), \tag{4.1}$$

where I is the interaction parameter, λ_z is the wavelength in the span, and T the period. Here we take the penetration length $\Delta^+ \approx 3$ (in wall units) as in the case of oscillatory excitation; later we will also investigate the effect of different values. Simulations performed at $Re_\tau \approx 150$ with different combinations of λ_z, T, I and Δ values show that drag reduction over 30% can be achieved in certain cases. We examine a representative number of cases next, and subsequently we present the modified near-wall structures.

4.1. *Effect of frequency*

Figure 10 shows the drag force history on the controlled wall for cases with $I = 1$ and $T^+ = 100, 50$ and 25, respectively. The results depend strongly on the frequency, even qualitatively, as in the case of the oscillatory Lorentz force discussed in the previous section. However, here $T^+ = 50$ gives the maximum drag reduction among the three cases, which is about 30%. This shows that for a travelling wave Lorentz force, we need to increase the frequency compared to the oscillatory Lorentz force (for the same amplitude) in order to achieve maximum drag reduction at about the same level.

4.2. *Effect of force magnitude*

The next simulations are performed with $\lambda = 5.6$, $T^+ = 100$ and $\Delta^+ = 3$. We have investigated three cases corresponding to force magnitudes $I = 0.5$, 1 and 2. Figure 11 shows the time history of the drag force on the lower controlled wall for the three cases. Surprisingly and unlike the results of Jung *et al*., the smaller the interaction parameter, the lower the drag force, with only $I = 0.5$ resulting in drag reduction. This finding is suggestive of favourable energetics for the travelling wave excitation.

4.3. *Effect of wavelength*

We investigate next the effect of spanwise wavelength by performing another set of simulations. We keep $T^+ = 50$, $\Delta^+ = 3$ and $I = 1$, and assign three different values of wavelength, i.e. $\lambda_z = 5.6$, 2.8 and 1.4 in global units (i.e. with respect to half-channel height). All three cases lead to drag reduction as shown in figure 12, with a monotonic trend, and with the longer wavelength corresponding to greater amount of drag reduction. This is true within the range tested (λ_z^+ up to 840 wall units) and no attempt was made to find the optimum wavelength due to limitations in computational resources.

4.4. *Effect of energy input*

In figure 10, where we presented the frequency effect for $\lambda_z = 5.6$, we now add one more curve (see figure 13*a*) corresponding to the case with $T^+ = 50$ and $I = 0.5$. We see that this new curve is very close to the curve corresponding to $T^+ = 25$ and $I = 1$, and for both simulations the total (average) energy input per cycle is the same. In particular, the product $I \times T$ is proportional to the energy input by the Lorentz force, and thus $I = 1, T^+ = 25$ has similar energy input to $I = 0.5, T^+ = 50$. To test this hypothesis further, we set $I = 2$ for $T^+ = 25$ and $I = 1$ for $T^+ = 50$ at time = 50

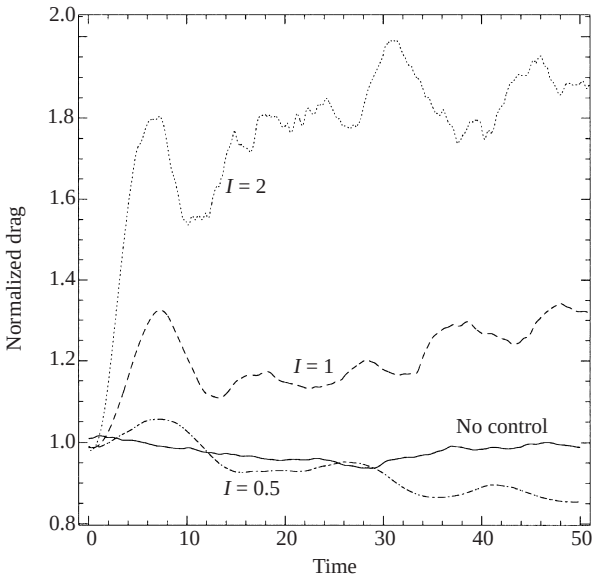

FIGURE 11. Effect of magnitude: time history of normalized drag force for $\lambda_z = 5.6$, $T^+ = 100$, $\Delta^+ = 3$ and $I = 0.5, 1, 2$.

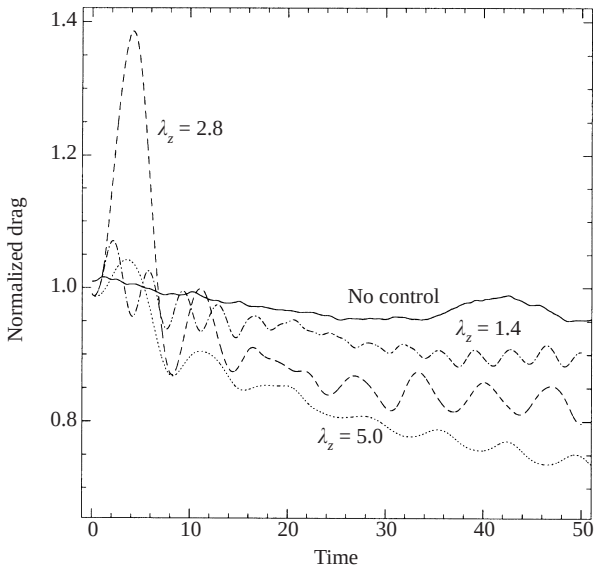

FIGURE 12. Effect of wavelength: time history of drag force for simulations with $\lambda_z = 5.6$, $T = 50^+$, $\Delta^+ = 3$ and different values of spanwise wavelength.

(in convective time units), and continue the simulations. Now both cases have the same average energy input as the case shown by the lowest curve in the plot. The new results are shown on figure 13(b). We can see that there is a sudden decrease at the beginning and eventually both curves follow each other closely towards the lowest curve in the plot.

Of course, not all combinations of (I, T^+) whose product is constant will produce the same flow result. For example, we have also carried out a simulation with $I = 0.25$

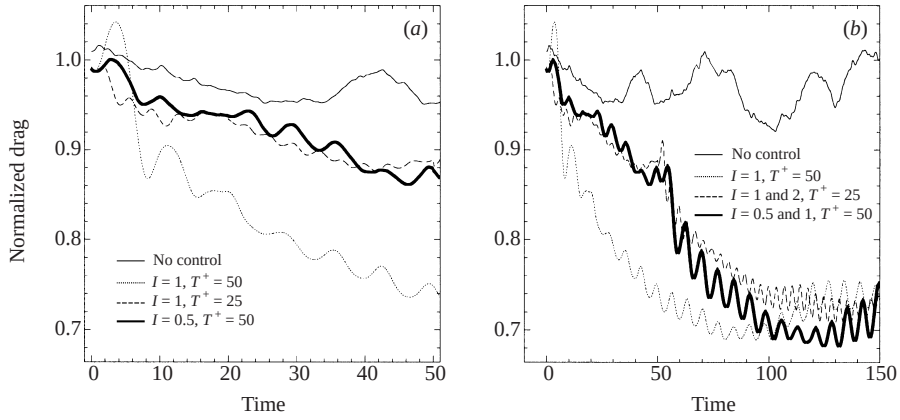

FIGURE 13. Effect of energy input: time history of normalized drag force for $\lambda_z = 5.6$ and different amplitude–frequency combinations.

and $T^+ = 200$ (with $\Delta^+ \approx 3$), but this case gives drag increase as the frequency of the travelling wave (and correspondingly the phase speed) is very low. This means that we first have to obtain the right range of frequency, and subsequently to search for the optimum energy input. The results here suggest that there is a threshold value of energy input, below which wall-turbulence is unaffected and above which drag increase may be obtained; close to that threshold large amounts of drag reduction can be achieved.

4.5. *Effect of penetration length*

We have examined the effect of penetration length by varying $\Delta^+ = 1.5$, 3, 6 and 15 for the cases summarized in table 1. Conclusively, we have found that if the product

$$I \times T^+ \times \Delta \approx 1 \tag{4.2}$$

then a drag reduction of about 30% is obtained independently of the specific values of I, T^+ and Δ but for deviations within a five-fold change in their magnitudes. This product is dimensional and its exact value depends on the Reynolds number. However, since all the simulations we present here are for fixed $Re_\tau \approx 150$ we will use it in the rest of the paper. Also, the values of the drag reduction are approximate as they depend on the modulation of drag history; we will return to this point later. In figure 14 we show typical time histories of three different combinations which result in approximately the same amount of drag reduction; the product $I \times T^+ \times \Delta = 1$ in all three cases. In figure 15 we show drag histories for a very small penetration length $\Delta = 0.01$ ($\Delta^+ \approx 1.5$) with one case corresponding to a product of 1 and the other to 0.5. These and other numerical experiments (not presented here) indicate the validity of this 'invariant product' of equation (4.2). It is a useful constraint since it can serve as a guide in designing physical systems that approximately satisfy equation (4.2). For example, in designing electro-magnetic tiles for actuation one has to select properly the electrode size as it influences directly the penetration length Δ.

4.6. *Effect of non-ideal travelling wave*

An ideal travelling wave excitation is difficult to implement in practice using electro-magnetic tiles or other micro-actuating devices (Ho 1997). In this section, we examine the consequences of such deviations from ideal travelling waves for drag reduction and suppression of turbulence production.

Δ	T^+	I	Product	Approx. drag change
$\frac{1}{50}$	50	1	1	−30%
$\frac{1}{25}$	50	1	2	0%
$\frac{1}{25}$	100	1	4	+70%
$\frac{1}{25}$	25	1	1	−30%
$\frac{1}{25}$	50	0.5	1	−30%
$\frac{1}{25}$	100	0.25	1	−30%
$\frac{1}{25}$	100	0.1	0.4	−25%
$\frac{1}{10}$	5	4	2	−10%
$\frac{1}{100}$	50	1	0.5	−20%
$\frac{1}{100}$	100	1	1	−30%

TABLE 1. Parameter values for DNS with sinusoidal travelling wave excitations.

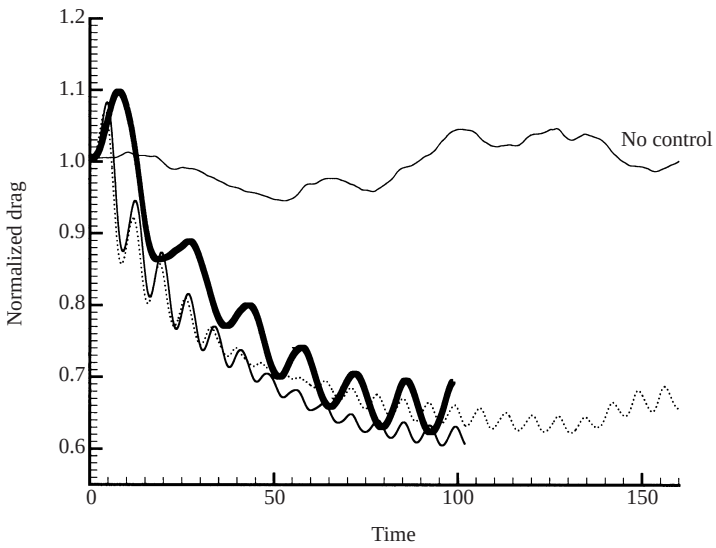

FIGURE 14. Effect of penetration length: time histories of normalized drag force for $\lambda_z = 5.6$ and different amplitude–period–penetration combinations with their corresponding product $I \times T^+ \times \Delta = 1$. Thick solid line: $(I = 0.25, T^+ = 100, \Delta = 0.04)$, dot line: $(I = 1, T^+ = 50, \Delta = 0.02)$, thin solid line: $(I = 0.5, T^+ = 50, \Delta = 0.04)$.

First, we model the spanwise component of the Lorentz force generated in the 16-phase multi-tile experiment at Princeton University, which was described in §2 (see figure 5). We can obtain the approximate waveform by examining the spanwise Lorentz force distribution in figure 16(*a*) (see p. 7), where we show a plan view of the configuration. Cutting through the centre of a pair of 'dots' across the channel, we obtain a cross-sectional view as shown in figure 16(*b*). This distribution resembles a generic 'two-bump' function shown in figure 17(*b*), which we use in the simulations. In figure 17(*a*), we present the time history of the drag force from our simulation. We can see that more than 25% drag reduction is obtained. However, this result is obtained with $T^+ = 25$; in fact, for $T^+ = 50$ we obtained a net drag increase. This

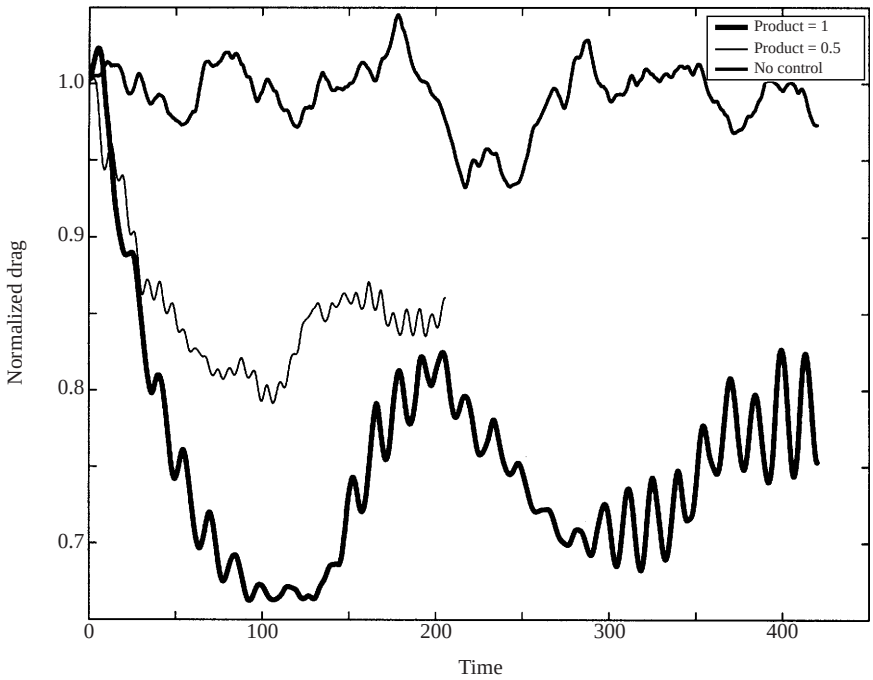

FIGURE 15. Effect of penetration length: Time histories of normalized drag force for $\lambda_z = 5.6$ and $\Delta^+ = 1.5$. The larger drag reduction curve corresponds to $I \times T^+ \times \Delta = 1$ and the lower drag reduction curve corresponds to $I \times T^+ \times \Delta = 0.5$.

suggests that in order to achieve drag reduction in this case, we need to sweep across the channel faster due to the gaps between the positive and negative action regions of Lorentz force.

We have also considered different waveforms which are discontinuous either in space or in time; these are summarized schematically in figure 18. We have found that for the square positive/negative pulse (plot *a*) we obtain a slightly higher drag reduction than in the case of the ideal sinusoidal waveform, but for the positive-only pulse (plot *b*) we obtain a slight drag increase. An interesting result was obtained with the piecewise step pulses shown in figure 18(*c*,*d*): For the waveform with an inactive zone around the node (plot *d*), a drag reduction of more than 20% is obtained whereas for the waveform without a node (plot *c*) no substantial change in the drag force was observed. The corresponding time histories of these two cases are shown in figure 19 along with the no-control case for reference. The parameters employed in all these simulations are $T^+ = 50$, $I = 1$ and $\Delta^+ = 3$; no attempt was made to explore this parameter space. In addition, for the two piecewise step pulses we employed a 'quantized' (i.e. non-continuous) time shifting in order to simulate more realistically the discrete temporal actuation of physical experiments.

4.7. *Modifications of near-wall structures*

In figure 20 we plot the mean velocity profile in viscous units; the shear velocity at the upper (no-control) wall is employed in the normalization. In figure 21 we present the velocity and vorticity turbulence intensities for the baseline case with $I = 1, T^+ = 50, \Delta^+ = 3$. The modified statistics near the controlled wall ($y = -1$) are similar to the statistics of the transverse oscillatory excitation (see figure 8). The

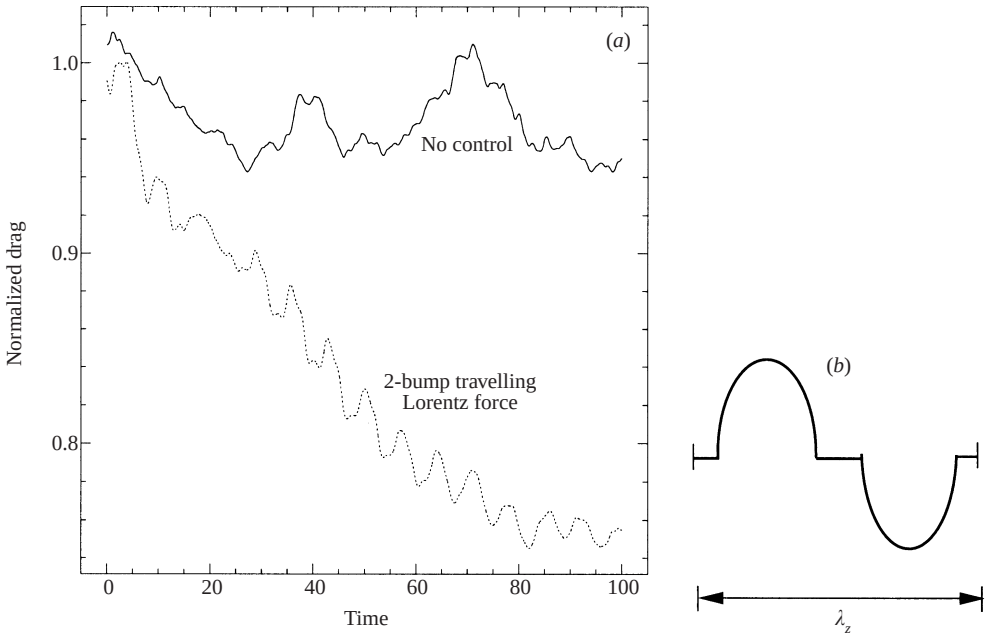

FIGURE 17. (a) Time history of normalized drag force with the 2-bump Lorentz force function shown in (b). $T^+ = 25, I = 1, \Delta^+ = 3$.

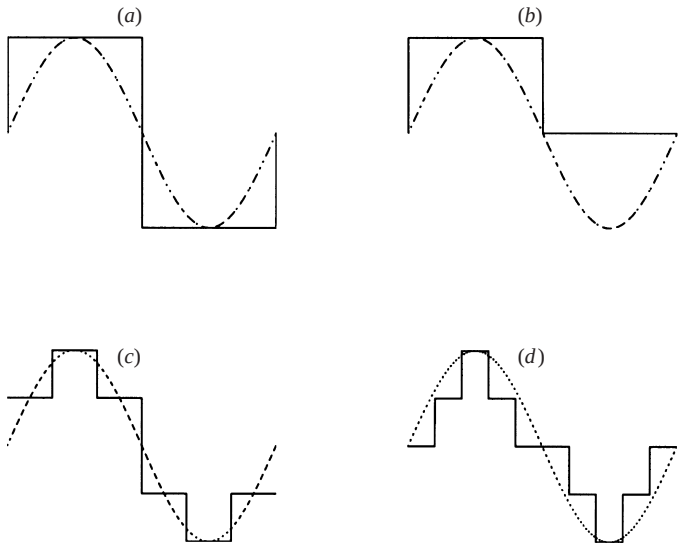

FIGURE 18. Generic non-ideal travelling waveforms.

maximum value of the spanwise r.m.s. velocity component is higher for the spanwise oscillations although the same amplitude of excitation ($I = 1$) is used in both cases. The streamwise r.m.s. vorticity achieves very large values at the wall because of the external source of vorticity introduced by the transverse force. This value (in global units) is 24 for the travelling wave and 28.5 for the spanwise oscillation case. All other turbulence intensities are lower on the controlled side, consistent with the drag reduction results. In figure 22 we plot the skewness factor for all velocity components

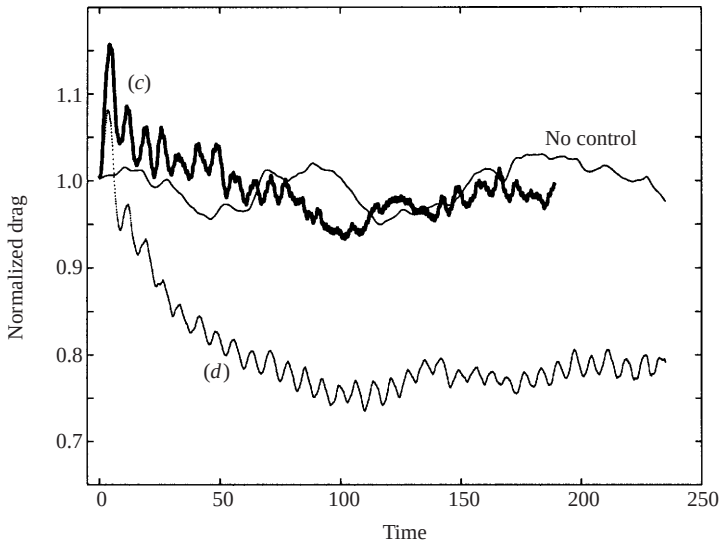

FIGURE 19. Time history of normalized drag force with the two piecewise step pulses of figure 18(*c*, *d*); $T^+ = 50, I = 1, \Delta^+ = 3$.

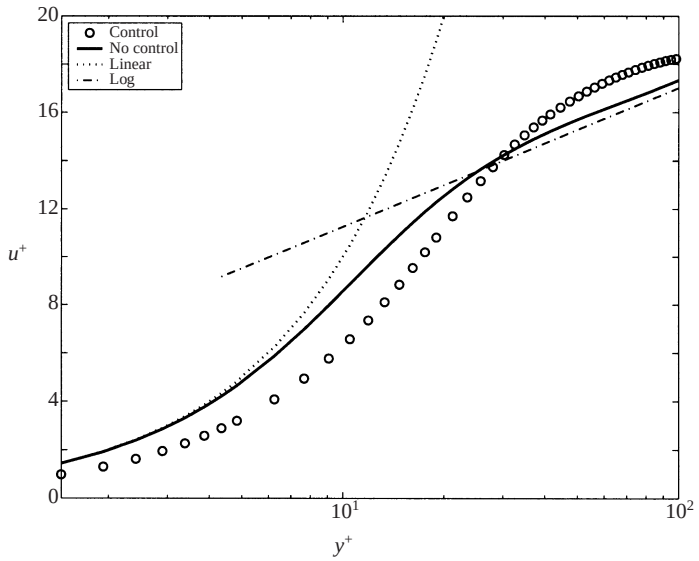

FIGURE 20. Mean velocity profile in viscous units for both controlled and uncontrolled flow. ($T^+ = 50, I = 1, \Delta^+ = 3$).

for both types of excitation, i.e. the travelling wave and the spanwise oscillation. The latter case exhibits substantially larger values for the streamwise and normal components but there are also qualitative differences very close to the controlled wall.

The main difference between the transverse travelling wave excitation and the transverse oscillatory excitation, as well as other drag reduction techniques such as riblets, spanwise oscillations, polymers etc. (see Gad-el-Hak 2000), is in the modification of near-wall streaks. The effect of the action of the travelling wave, when it is effective in reducing the drag force on the controlled wall, is to weaken and in many cases to

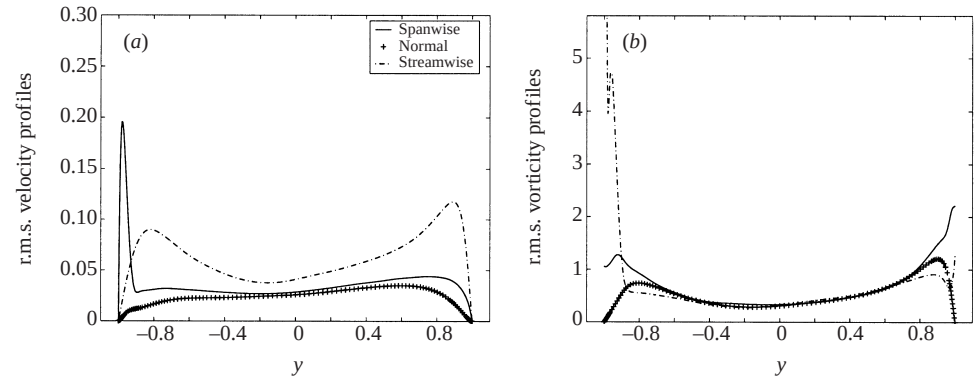

FIGURE 21. Velocity (a) and vorticity (b) turbulence intensities across the channel. ($T^+ = 50, I = 1, \Delta^+ = 3$) (global units).

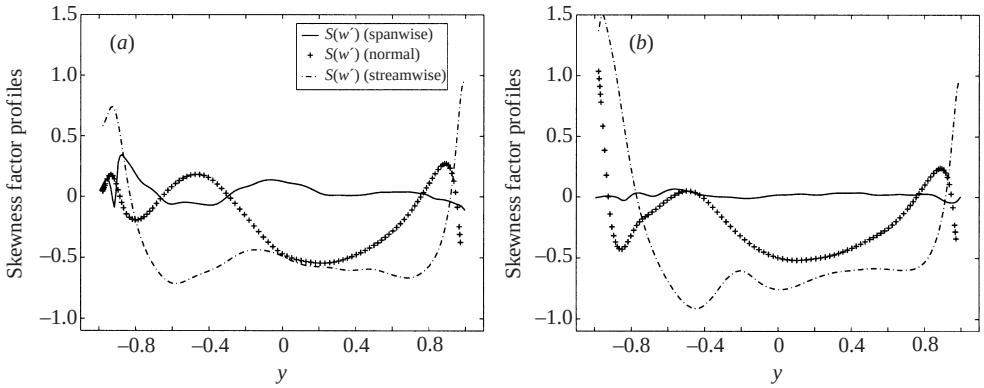

FIGURE 22. Skewness factor for all velocity components. (a) Travelling wave excitation corresponding to $T^+ = 50, I = 1, \Delta^+ = 3$; ($b$) spanwise oscillatory excitation corresponding to $T^+ = 100, I = 1, \Delta^+ = 3$.

eliminate most of the wall streaks. This is shown in figure 23 that plots instantaneous near-wall streamwise velocity contours both at the controlled lower wall (plot b) and at the upper uncontrolled wall (plot a) at the same time instant; these planes are at $y^+ = 4$ away from the walls. We see that while the upper wall exhibits the familiar turbulence structure consisting of pairs of high-speed and low-speed streaks with the characteristic spacing of about 100 wall units, no such pairs can be found near the controlled surface. Instead, a wide 'ribbon' of low-speed velocity is formed. This is a significant new finding, in view of the fact that streaks and streak spacing are usually difficult to alter even in cases where a very large amount of drag reduction has been obtained. For example, in drag reduction using polymers the increase in streak spacing is proportional to the percentage of drag reduction (Tiederman 1990; Sureshkumar, Beris & Handler 1997; Nieuwstadt & DenToonder 2001).

In order to contrast this finding with the turbulence structure resulting from other drag reducing techniques, we plot in figure 24 the wall streaks visualized in simulations of turbulent flow over streamwise riblets (Chu & Karniadakis 1993). Although a drag reduction of about 5% is achieved in this case, the lateral spacing of the streaks does not change but the streaks appear more elongated compared to the uncontrolled case. For randomly distributed roughness a larger amount of drag reduction is achieved

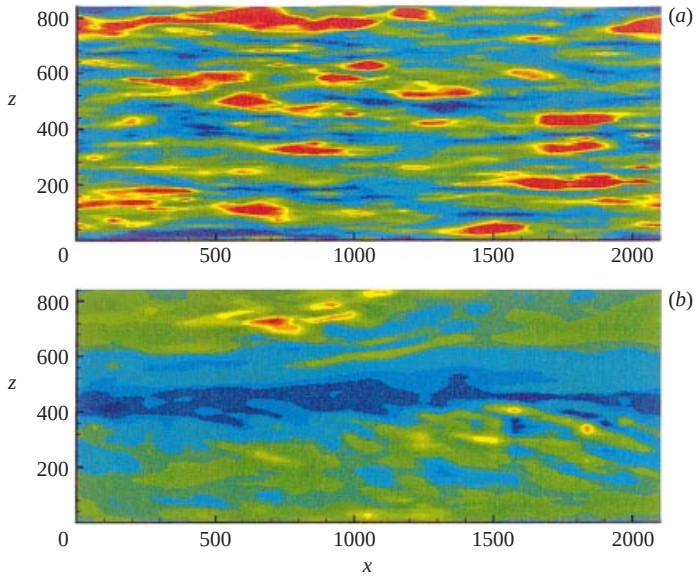

FIGURE 23. Instantaneous flow visualizations of wall streaks. (*a*) no-control; (*b*) travelling wave excitation corresponding to $I = 1$, $\lambda_z^+ = 840$ and $T^+ = 50$; $L_z^+ = 840$. Blue colour indicates low-speed streaks and yellow-red high-speed streaks.

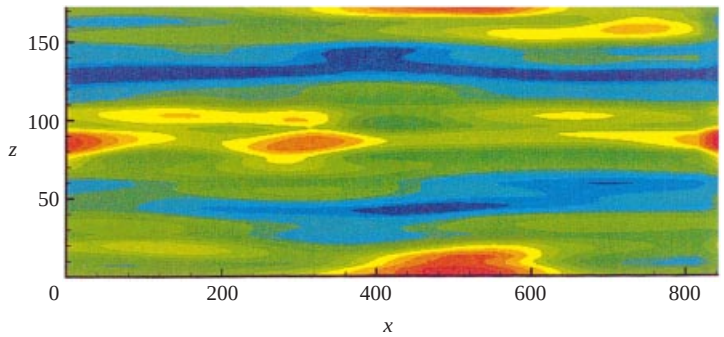

FIGURE 24. Instantaneous streamwise velocity contours near a wall mounted with riblets. $L_z^+ = 200$. Blue colour indicates low-speed streaks and yellow-red high-speed streaks.

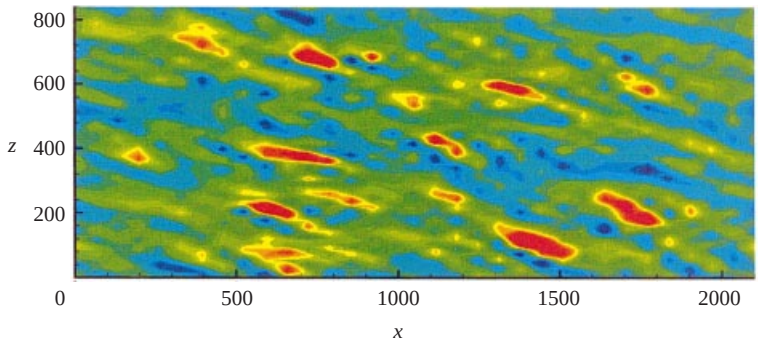

FIGURE 25. Streamwise velocity contours near a wall controlled by an oscillatory force along the spanwise direction; $T^+ = 100$. $L_z^+ = 840$. Blue colour indicates low-speed streaks and yellow-red high-speed streaks.

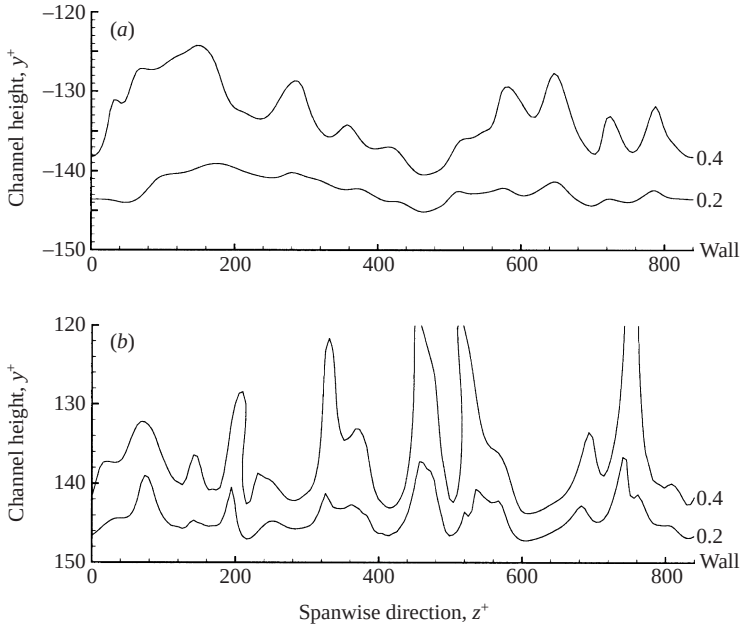

FIGURE 26. Instantaneous streamwise velocity contours on a cross-flow plane for the controlled wall (*a*) and the uncontrolled wall (*b*).

with the spacing of the streaks increased by about 10% (Sirovich & Karlsson 1997). Similarly, if instead of a travelling wave an oscillatory flow along the spanwise direction is imposed, as discussed in § 3, the wall streaks are still present as shown in figure 25, but they are inclined with respect to the flow direction due to the spanwise flow component. In both cases, despite these obvious modifications the fundamental structure of near-wall streaks and corresponding vortex lines remain the same, unlike the travelling wave excitation, where no wall streaks or vortex lines resembling hairpin vortices can be found.

In order to investigate the spatial extent of the modification of flow structures in the near-wall regions, we visualized instantaneous contours of streamwise velocity as well as pressure. In figure 26 we present two contour levels of the streamwise velocity in a cross-flow plane for both the controlled and uncontrolled wall. We see that even at distances more than 20 wall units away from the controlled wall there are no streaks present as in the uncontrolled case. To obtain a magnitude of the intensity of the streaks we plot in figure 27 one level of the normal vorticity for the controlled and uncontrolled wall. These results too confirm the significant weakening of streaks even away from the wall in the controlled case and the complete elimination of most of the wall streaks. Of course, not all streaks are eliminated, otherwise turbulence could not be sustained (Jimenez & Pinelli 1999).

In figure 28 we plot four different quantities (streamwise velocity, streamwise vorticity, pressure and spanwise velocity) close to the controlled wall ($y^+ = 4$) all at the same time instant. In particular, we observe that the spanwise velocity has a travelling wave form similar to the excitation force, which results in the 'regularization' of the streamwise vorticity. Indeed, unlike the classical view where reinforcement of the *spanwise* vorticity may result in suppression of turbulence production (see for example Nosenchuck & Brown 1993), here it is the introduction of external *streamwise* vorticity

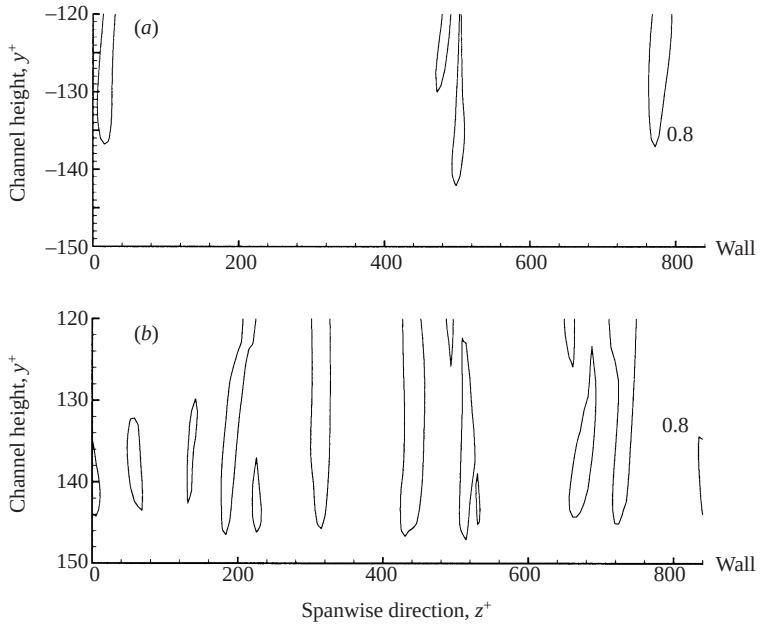

FIGURE 27. Instantaneous normal vorticity contours on a cross-flow plane for the controlled wall (*a*) and the uncontrolled wall (*b*).

that leads to suppression and significant weakening or substantial elimination of the near-wall pairs of streaks. This regularization of streamwise vorticity has also been suggested by Dhanak & Si (1999) as the mechanism for drag reduction in spanwise wall oscillations. However, a different explanation has been provided by Choi (2000) who proposed that the total streamwise vorticity is weakened substantially over one oscillation period because of a change of sign of the vorticity introduced by the vortex sheet sustained by the periodic Stokes layer. At the same time the net spanwise vorticity is enhanced.

Returning to the travelling wave excitation, we also see in the plots of figure 28 that the wide 'ribbon' of low-speed fluid, which extends over 200 units, is directly related to the large strip of positive streamwise vorticity (red zone on figure 28*b*). The underlying mechanism in the travelling wave excitation seems to be related to the stabilization of the near-wall streaks (Swearingen & Blackwelder 1987). It can possibly be explained by the more recent theories on regeneration mechanisms of near-wall turbulence put forward by Jimenez & Pinelli (1999), Schoppa & Hussain (1997) and Waleffe (1997). The results by Schoppa & Hussain (1998), in particular, are similar to our results although the control strategy is different. Specifically, they use a lower-amplitude standing wave type of excitation which is applied throughout the domain, in contrast to the excitation employed here which is restricted to a very thin layer near the wall. However, both their strategy and the transverse travelling wave aim at stabilizing the near-wall streaks. In both approaches, the vorticity fluctuations normal to the wall are reduced by at least a factor of two compared to the no-control case for drag reducing cases (see figure 21). It was also found in a model postulated by Schoppa & Hussain (1997) that the normal vorticity ω_y is a key indicator of formation of new streamwise vortices near the wall by streak instability. Specifically,

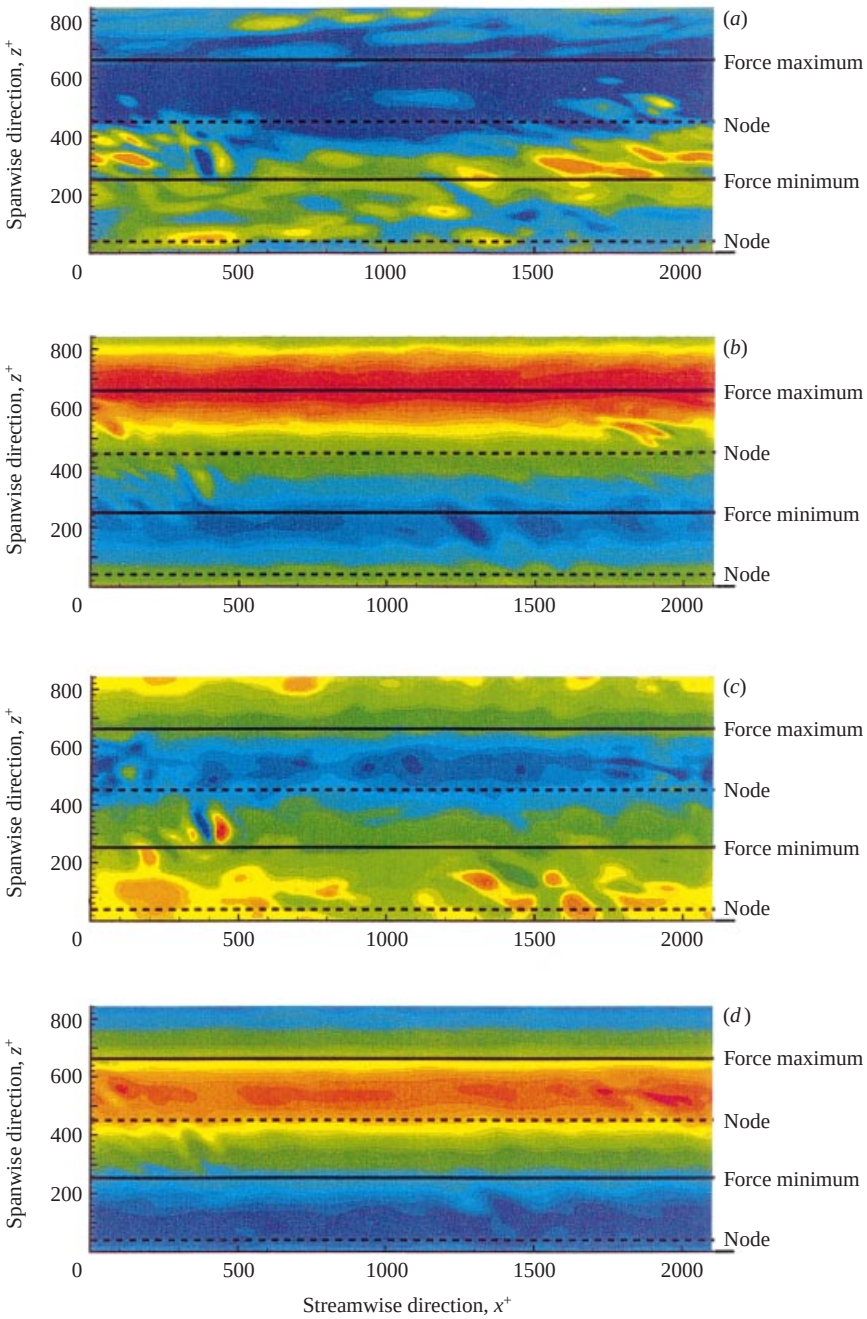

FIGURE 28. Visualization of instantaneous streamwise velocity (a), streamwise vorticity (b), pressure (c), and spanwise velocity (d) at a distance $y^+ = 4$ from the wall controlled by a transverse travelling wave. Red denotes high values and blue denotes low (or negative) values. All data correspond to time point B in figure 29.

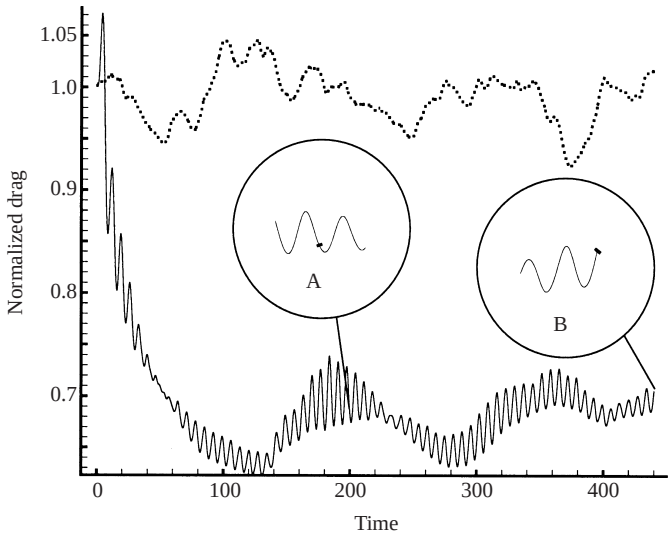

FIGURE 29. Baseline case: time history of normalized drag force for $\lambda_z = 5.6, I = 1, \Delta^+ = 3$ and $T^+ = 50$. Time is in global units. The no-control case is denoted by the dotted line.

the growth rate of the streaks sinous instability mode grows with the magnitude of ω_y, so if it falls below a threshold no such instability occurs.

The role of the streamwise vorticity ω_x is also of great interest. In figure 28(b) we plot instantaneous contours of streamwise vorticity for a drag reducing case with the wavelength equal to the span of the domain (i.e. $\lambda_z = 5.6$). We see that ω_x is also a travelling wave that forms a protective shield for the controlled surface. With the introduction of external streamwise vorticity which is proportional to

$$\frac{I}{\Delta} e^{y/\Delta} \sin\left(\frac{2\pi}{\lambda_z} z - \frac{2\pi}{T} t\right)$$

in the near-wall region, the streamwise vortices are significantly strengthened. This enhancement of the streamwise vorticity and associated streak stabilization has also been found numerically by Jimenez & Pinelli (1999) (see their figure 10). Specifically, they filtered explicitly the coherent component of the normal vorticity component by multiplying it by a filter function. As the filter width increases so does the streamwise vorticity while at the same time there is significant streak damping with eventual re-laminarization of the flow. The drag reduction obtained in these simulations was about 30% before an abrupt transition to flow laminarization occurred with sudden drop in all turbulence intensities. A comparison of the corresponding velocity and turbulence statistics (figure 21 here) with figure 10 of Jimenez & Pinelli reveals many similarities before the flow returns to a laminar state under strong filtering.

Finally, we discuss the phase relationship between the flow structures and the imposed travelling wave excitation. In figure 28 we have superimposed the position of the maximum, minimum and the node for the external force at that time instant. The relative phase between the force and the flow varies in time, and this is responsible for the significant drag modulation. In figure 29 we plot the long time history of the baseline drag reducing case ($I = 1, T^+ = 50, \Delta^+ = 3$), where we clearly see a modulation with relatively large period.

We focus on two specific time instants, as marked in the figure, in order to compare

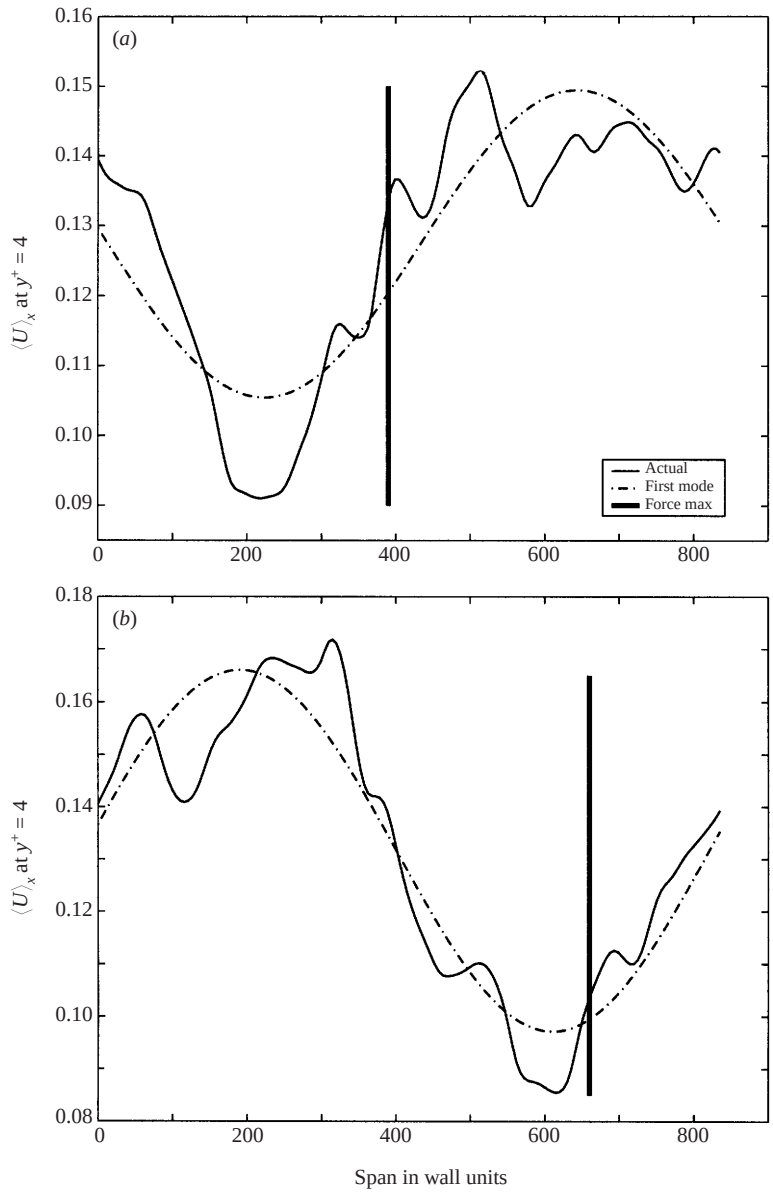

FIGURE 30. Instantaneous flow velocity averaged along the streamwise direction ($y^+ = 4$): (a) time $t = 200$ (point A) and (b) time $t = 440$ (point B) in figure 29.

corresponding flow structures. In the first one (point A) a local (in time) drag decrease is obtained and the corresponding streaks are visualized in figure 30(a). This is the time instant of point A in figure 29. Specifically, we plot the first Fourier mode of the streamwise velocity at $y^+ = 4$ along the span. The vertical line denotes the location of the force maximum at that time instant, while the dot-dash line corresponds to the first mode of the streamwise velocity. A similar plot is shown in figure 30(b) but at a later time corresponding to a local (in time) drag increase (point B). By comparing the phase between the maximum of the external force and the maximum of the filtered streak curve, we observe the following: at $y^+ = 4$ the maximum of the first mode of

the streaks and the Lorentz force maximum (figure 30) are at phase difference always in the interval $[\pi/2, \pi]$. Specifically, we observe that at a time instant of *drag decrease* this difference approaches the lowest value $(\pi/2)$, whereas at a time instant of *drag increase* this difference approaches the highest value (π).

In addition, there is a slight phase difference between the drag force and the excitation force. For the baseline reducing case ($I = 1, T^+ = 50, \Delta^+ = 3$) the period (in viscous units) of the drag force was estimated close to 46. This shows that there is a difference of 4 viscous time units between the period of the excitation force and the period of the drag force. This explains the beating phenomenon observed in the figure 29 of the drag history plot.

5. Summary and discussion

The main result of this paper is that travelling waves of appropriate form propagating along the spanwise direction and within the viscous sublayer of a turbulent boundary layer may stabilize the wall-streak instability, suppress turbulence production, and lead to large amounts of drag reduction.

Moreover, we have identified the amount of energy input that is required to produce the desired drag reduction effect. Such travelling waves have also been observed in the EMTC experiments at Princeton by Nosenchuck and collaborators, but at an oblique direction of about 45° with respect to the spanwise direction (Nosenchuck, private communications). Their result indicates the presence of a significant streamwise Lorentz force component. Indeed, for the EM tile array studied in § 2, the Lorentz force component at a fixed time instant has the distribution shown in figure 31 and magnitude comparable to the spanwise component. DNS studies with a streamwise Lorentz force having the form of a travelling wave result in drag increase as shown in figure 32, which is consistent with previous experimental and numerical studies (Henoch & Stace 1995; Crawford & Karniadakis 1997). However, if a small streamwise component, e.g. 10% of the spanwise force, is superimposed on the (ideal) spanwise forcing then there is no adverse effect on the drag reduction. As the streamwise excitation increases relatively to the spanwise excitation then a gradual degradation of performance occurs. At an amplitude of about 50% no drag reduction occurs and at higher amplitudes the drag force increases compared to the uncontrolled case.

Given the findings of the present study, the EM tiles in Nosenchuck's array can be re-designed so that a predominantly spanwise Lorentz force is produced. To this end, the square electrodes need to be replaced by thin elongated electrodes with aspect ratio of at least ten, or even electric wires, to produce the desired effect. Preliminary computations using Maxwell's equations support this proposal. Another parameter that determines the net amount of drag reduction is the penetration length Δ in equation (4.1). For given values of I and T^+ we found that if Δ is obtained from

$$\Delta \approx (I \times T^+)^{-1}$$

(in global units) then the largest drag reduction is obtained. We found that for $\Delta^+ > 15$ a drag increase is obtained but this may be an artifact of the channel domain and it may not be true in boundary layer flows where there is no upper wall to induce artificial flow structures.

The relatively small penetration Δ of the excitation force into the fluid suggests several *surface-based* techniques as cost-effective actuation candidates. Moreover, the simulation results show that large values of the amplitude I are not necessary to obtain

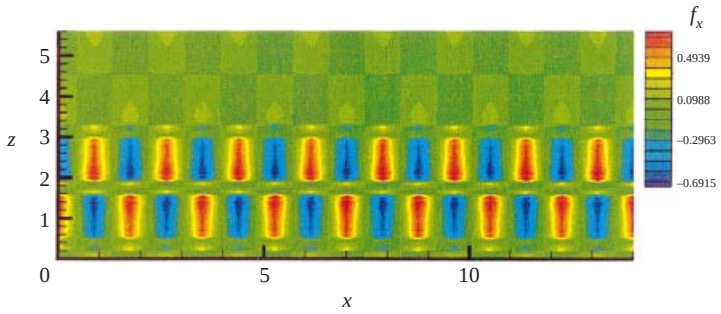

FIGURE 31. Contours of the instantaneous streamwise Lorentz force during one phase in the 16-phase Princeton experiment (plan view). The domain dimensions are in global units.

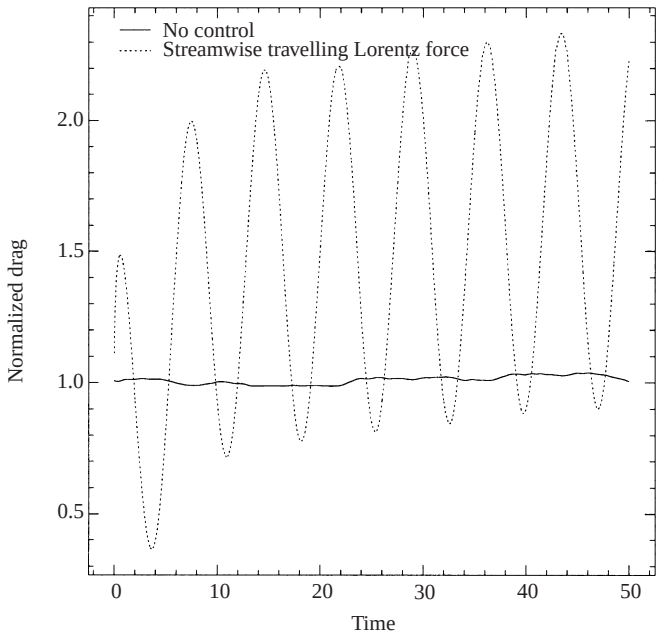

FIGURE 32. Streamwise excitation: time history of normalized drag force corresponding to $I = 1$ and $T^+ = 50$. Time is in convective units.

drag reduction. For example, we have found that at a period $T^+ = 100$, excitations with $I = 1$ and $I = 2$ lead to drag increase but $I = 0.5$ leads to drag decrease; we have also shown that $I = 0.1$ is very effective. These values of interaction parameter I are in global units and thus they depend on the Reynolds number; no attempt was made in this study to obtain such scaling. From the implementation point of view, unlike other methods proposed for wall-streak control where individual streaks are controlled, the characteristic length scale here is of the order of tens of wall-streak spacings, i.e. 1000 wall units or more. Indeed, the simulation results suggest a monotonic increase of the amount of drag reduction in the wavelength range tested, from $\lambda_z^+ = 210$ to $\lambda_z^+ = 840$.

We now examine the feasibility of this technique in realistic flow environments. Let us first consider flow around a Remotely Operated Vehicle (ROV) with typical Reynolds number of 10^6 and boundary layer thickness of 5 mm. Based on the set

of non-dimensional parameters obtained in the simulation, an appropriate range for the dimensional wavelength and pulsing frequency is 20 mm and 50 Hz, respectively. For submarines with typical Reynolds number of 10^8 the required wavelength is approximately 2 mm and the frequency 5 KHz. For aerodynamic applications at similar conditions, the wavelength is an order of magnitude larger and the frequency an order of magnitude lower. These values suggest that the proposed method can be implemented by a variety of techniques, especially in the context of MEMS technologies (Ho 1997), i.e. via micro-actuators or via morphing surfaces. The latter involves the creation of 'smart skin' that can be 'cast and pasted' on existing vehicles with minimal intrusion. This smart skin is based on actuators of small size and significant force, such as piezoceramic and magneto-restrictive materials (Near 1996) as well as shape memory alloys (SMA) (Rediniotis, Lagoudas & Wilson 2000). Piezoceramic actuators can produce up to 1 cm displacement and respond up to the 20 KHz frequency range at 100 V driving voltage. Therefore, they are more appropriate in the very high Reynolds number regime. On the other hand, SMAs are more efficient and work well in the lower Reynolds number regime as in ROV applications. In fact, there has been a successful demonstration of SMA-driven control by Rediniotis and collaborators in similar conditions (Rediniotis *et al.* 2000). It has been shown that per 10 cm of strip width, a single SMA wire of 0.03 in. producing a force of 20 N is sufficient to produce the desired travelling wave pattern. The overall efficiency of piezoelectric or SMA actuation is not known but in general the latter requires less driving voltage. In particular, our finding that even at $\Delta^+ \approx 1.5$ a drag reduction of more than 25% is achieved suggests that the required surface displacements can be obtained with modest voltages.

This work was supported initially by DARPA and Naval Undersea Warfare Center, and subsequently by DARPA's Micro Adaptive Flow Control program. We would like to thank D. Nosenchuck for providing information on his experiments, and K. Breuer, J. Paduano and Jin Xu for helpful discussions. We would like to dedicate this paper to the memory of Prof. Linda Krall with whom we had very valuable discussions on turbulent drag reduction during the initial phase of this project.

Appendix A. Simulation versus experiment

A.1. *Force modelling*

We show in this section that the magnetic field can be modelled very accurately using detailed measurements obtained from an experiment, which was especially designed for this purpose at the Naval Undersea Warfare Center (NUWC) for a single electromagnetic tile. However, as there are no available experimental data for the electric field, uncertainties in the Lorentz force modelling may be due to errors in modelling the electric field.

A.1.1. *Magnetic field modelling*

We employ the laws of induction (Jackson 1975) to calculate the magnetic potential Φ_B:

$$\Phi_B(\boldsymbol{x}) = \frac{\mu_M}{4\pi} \oint_S \frac{\boldsymbol{n}' \cdot \boldsymbol{M}(\boldsymbol{x}')\mathrm{d}x'}{|\boldsymbol{x} - \boldsymbol{x}'|}, \tag{A 1}$$

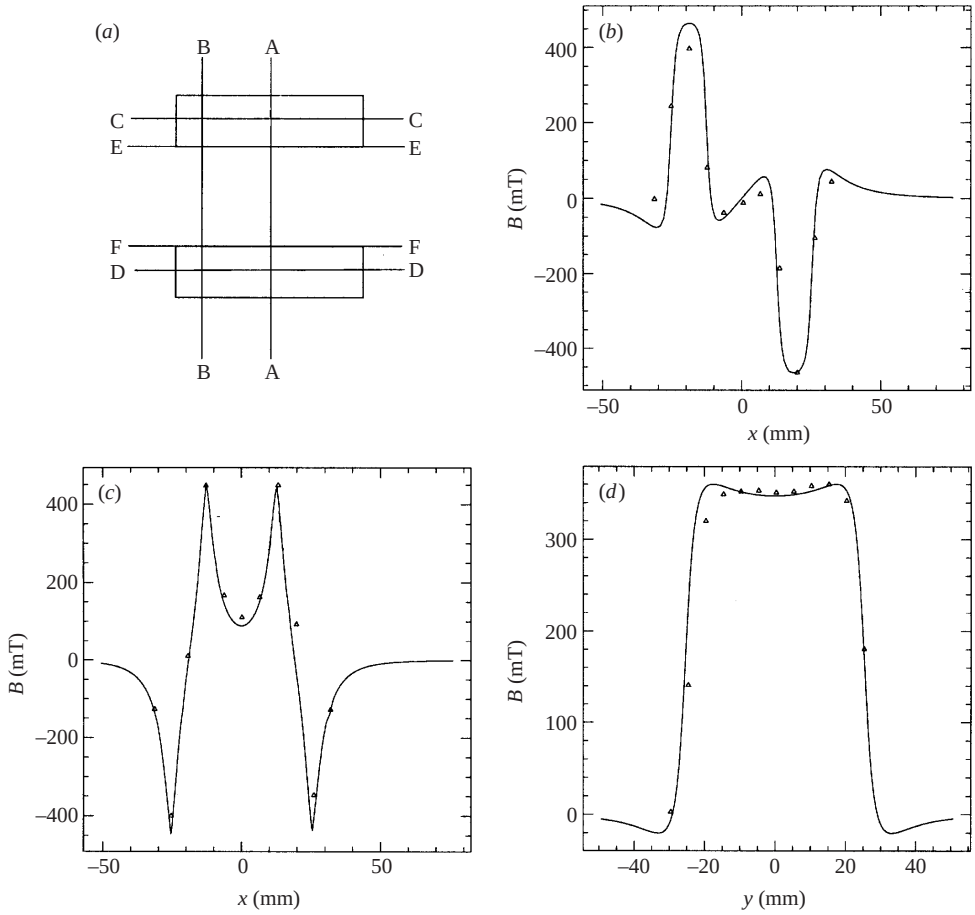

FIGURE 33. (*a*) Positions of profiles taken; (*b*) normal component of B along A–A line, 1 mm above tile; (*c*) streamwise component of B along A–A line, 1 mm above tile; (*d*) normal component of B, along E–E line, 1 mm above tile. The flow direction is along the longer side of the magnets. The experimental results (symbols) are due to R. Philips, NUWC.

where S is the surface of magnets, $\boldsymbol{n}$ the unit normal to S, and $\boldsymbol{M}$ the permanent magnetization. This corresponds to solving

$$\nabla^2 \Phi_B = 0 \quad \text{in } \Omega \tag{A 2}$$

with Neumann boundary conditions, i.e.

$$\left.\frac{\partial \Phi_B}{\partial n}\right|_{\partial\Omega} = \boldsymbol{n} \cdot \boldsymbol{M}, \tag{A 3}$$

where $\partial\Omega$ is the surface of the permanent magnet, Ω is the region outside the magnet, and $\boldsymbol{n}$ is the unit normal vector for $\partial\Omega$. We compute the magnetic field using $M = 1$ first, and then since the problem is linear, we scale it with a constant so that the maximum value of magnetic induction (value of $\boldsymbol{B}$ in the normal direction), matches the maximum experimental value (Du 1999). In figure 33 we present some representative results of a very detailed comparison for the NUWC tile; the complete results can be found in Du (1999).

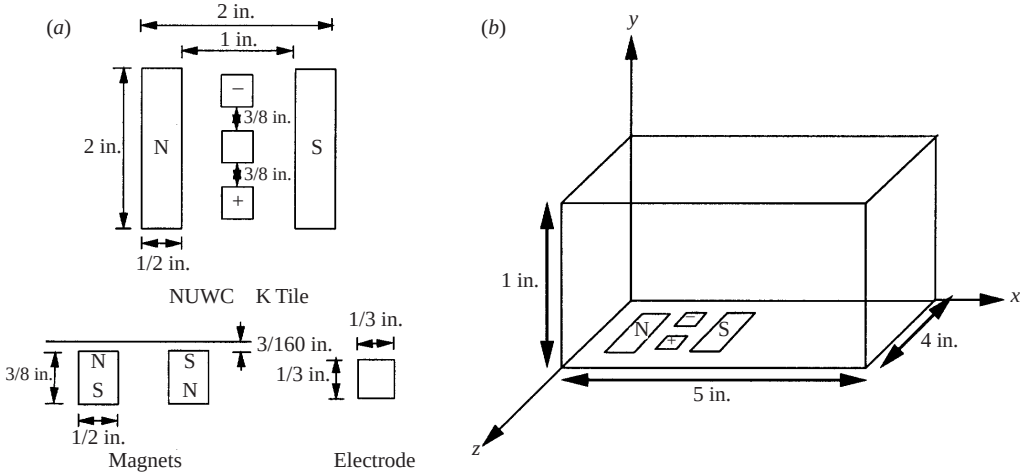

FIGURE 34. (*a*) NUWC K tile geometry (plan and side views); (*b*) computational domain. Flow is along the *x*-direction.

A.1.2. *Electric field modelling*

The electric field can also be obtained from the electric potential that obeys Laplace's equation:

$$\nabla^2 \Phi_E = 0, \quad \boldsymbol{E} = -\nabla \Phi_E, \tag{A 4}$$

For a highly conducting medium, $\boldsymbol{E} = 0$ (in/on the medium), and thus Φ_E is approximately constant on the electrode surface. However, this approximation is inaccurate due to electrode edge effects and the so-called Motz problem (Motz 1946). Thus, we computed first the charge $\sigma(\boldsymbol{x})$ and subsequently the potential on the electrode (see Du 1999). To this end, we used the code FASTCAP (Nabors, Kim & White 1992), which employs a boundary integral formulation, i.e.

$$\Phi_E(\boldsymbol{x}) = \oint_S \frac{\sigma(\boldsymbol{x}')\mathrm{d}x'}{|\boldsymbol{x} - \boldsymbol{x}'|}, \tag{A 5}$$

where S is the surface of electrodes. Having obtained Φ_E we employ spectral/hp element methods (Karniadakis & Sherwin 1999) with p-refinement to obtain the entire field accurately.

It is worth mentioning that the most efficient way to compute the electric field is to solve directly equations (A 4). This is not necessary in the single tile case, but it is in the multi-tile case where using FASTCAP requires much more computational time; thus, we adopted the following method. As already mentioned, setting the potential equal to a constant (hence $\boldsymbol{E} = 0$) is not correct because of electrode edge effects. One way around this problem is to use the solution obtained from FASTCAP to approximate the appropriate (variable) Dirichlet boundary conditions for electric potential that should be set over electrodes. In regions without electrodes a zero Neumann condition is imposed. The results obtained using this mixed approach agrees very well with that obtained entirely from FASTCAP (Du 1999).

A.2. *Velocity comparisons*

A more detailed analysis and comparison of velocity fields has been presented in Du, Beskok & Karniadakis (1999), including the case of an impulsive excitation via a single electromagnetic tile (see also Donovan, Kral & Cary 1997). Here, we summarize

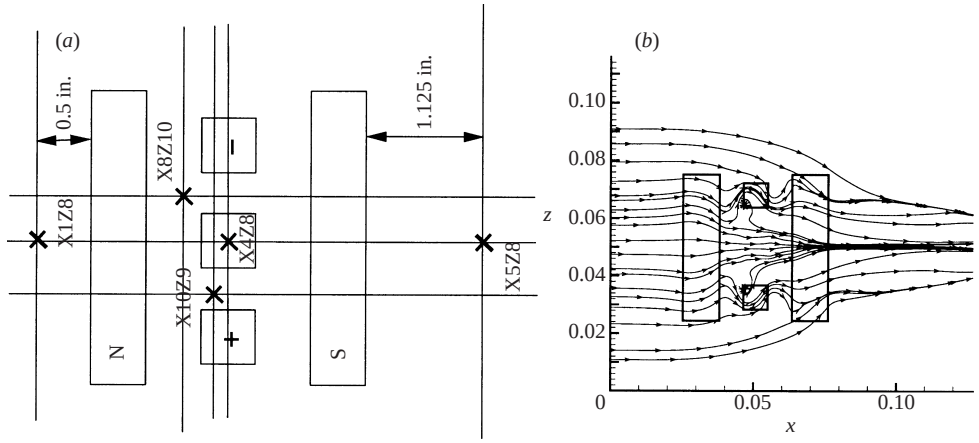

FIGURE 35. (*a*) Locations where data is taken; (*b*) streamlines taken very close to the wall: $y = 10^{-5}$, $U = 0.2\,\mathrm{m\,s^{-1}}$, time = 1.325.

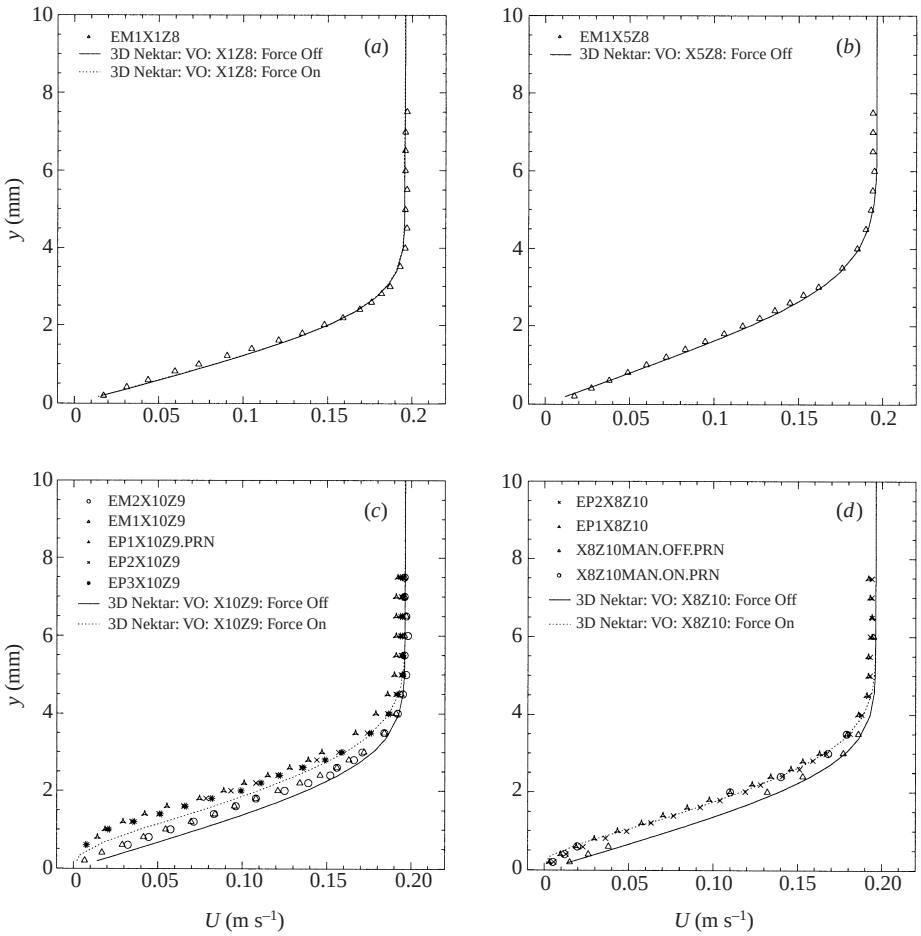

FIGURE 36. (*a*) X1Z8; (*b*) X5Z8; (*c*) X10Z9; (*d*) X8Z10. The solid line corresponds to the no-control case and the dot line to the controlled case. The experimental results (symbols) are due to R. Philips, NUWC.

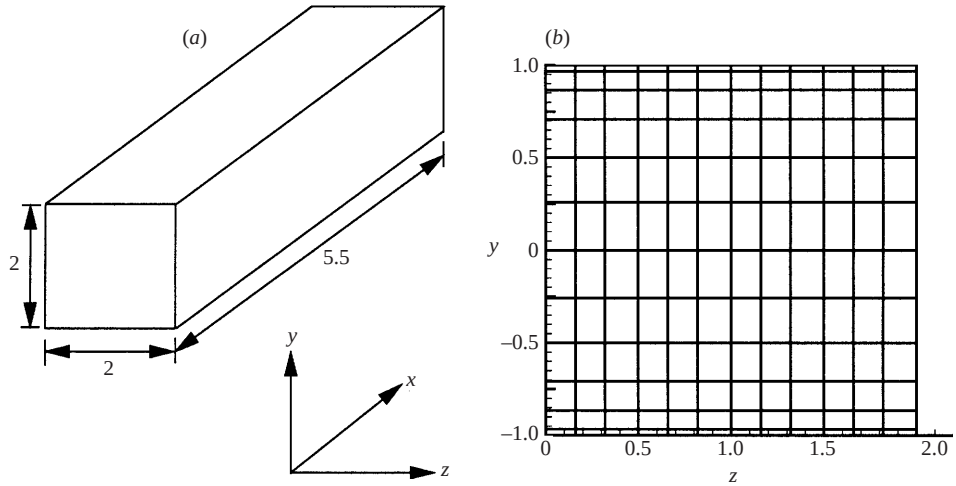

FIGURE 37. (*a*) Small computational domain with 144 elements; (*b*) a 'slice' of the mesh in the crossflow direction.

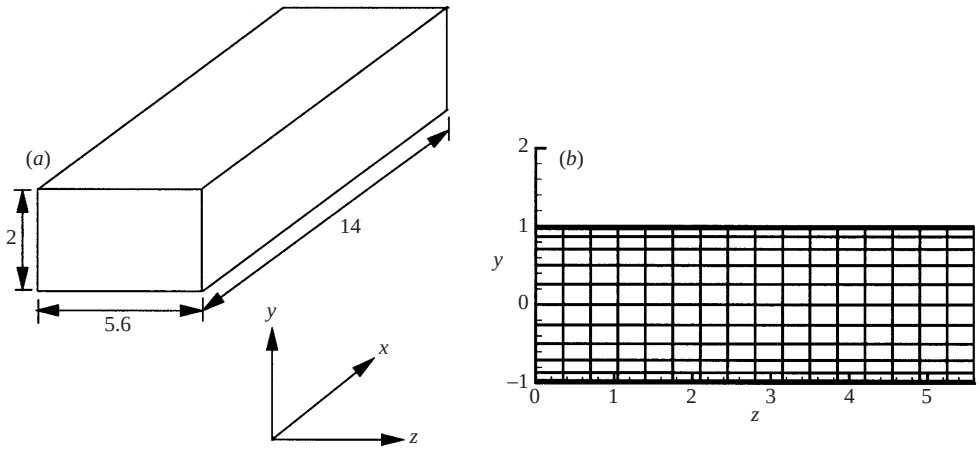

FIGURE 38. (*a*) Large computational domain with 192 elements; (*b*) a 'slice' of the mesh in the crossflow direction.

the results from a comparison with an experiment of a single tile actuation and inflow velocity $U = 0.2\,\mathrm{m\,s^{-1}}$. All simulations were run with the spectral/hp element code $\mathcal{N}\varepsilon\kappa\mathcal{T}\alpha r$ (Karniadakis & Sherwin 1999). The geometry of the tile and the computational domain are shown in figure 34.

We first establish a steady boundary layer flow with the inflow velocity profile matching that of the experiment. Then, we turn on the Lorentz force and run the simulation until the flow is steady. In figure 35, we indicate the locations where measurements are taken and we plot streamlines very close to the wall. We see that the flow is converging towards the centre of the tile, and that strong vortices are induced at the electrode edges. In figure 36 we plot streamwise velocity profiles taken at positions where the experimental data are also taken. We see that before the force is turned on, at locations both upstream (X1Z8) and downstream (X5Z8) of the tile, the simulation results match quite well with experiment. At locations X10Z9 and X8Z10, where experimental data are also available for the 'force-on' comparison, the

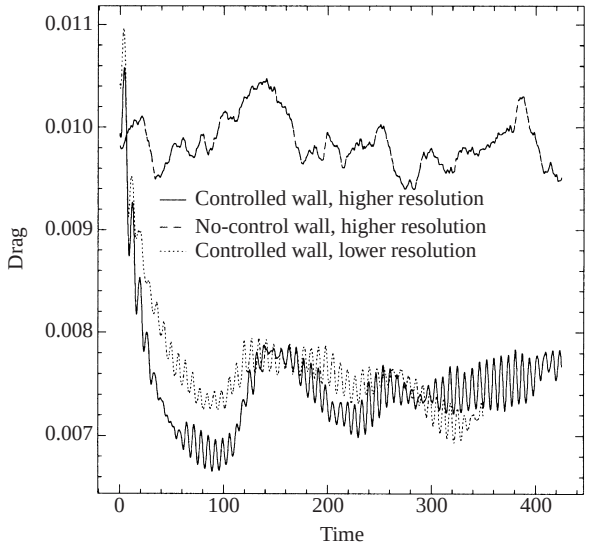

FIGURE 39. Resolution study for travelling wave. Time history of drag force for high resolution and low resolution. The no-control case is also represented.

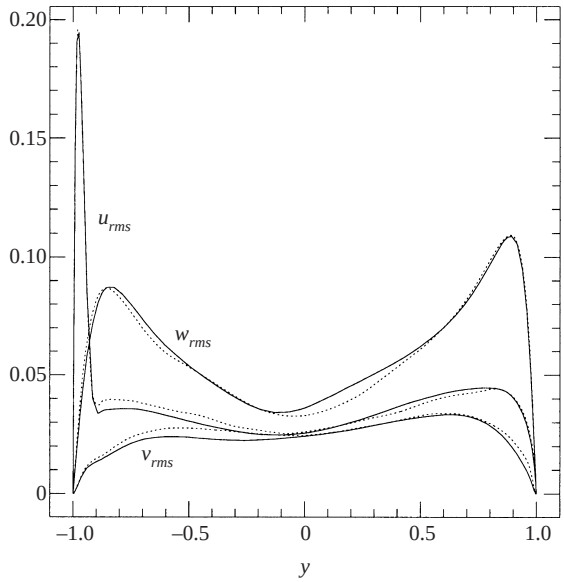

FIGURE 40. Resolution study for travelling wave: turbulence intensities are shown; solid line represents high resolution and dot line represents lower resolution.

matching is equally good for instances both before and after the Lorentz force is turned on.

Appendix B. Simulation parameters and resolution studies

All flow simulations were done using the parallel code $\mathcal{N}\varepsilon\kappa\mathcal{T}\alpha r$ (the PRISM version), which is based on spectral/hp element methods (Karniadakis & Sherwin

1999). Extensive resolution studies and benchmarks of this code for turbulent channel flows have been performed by Crawford (1996) and Crawford *et al.* (1996).

Two computational domains were employed in the simulation shown in figures 37 and 38; also included are the corresponding meshes consisting of 144 and 192 elements, respectively. Fourier expansions were employed along the streamwise x-direction. Simulations were performed on both meshes with polynomial order varying from $p = 7$ to $p = 11$, and the number of Fourier modes varying from 16 to 64. Typical results from the comparison between low and high resolution in figure 39 show that essentially the same drag reduction is predicted by both simulations. However, there is some difference in instantaneous values and especially in the initial reduction rate. The corresponding differences in turbulence intensities between the low- and high-resolution runs are small as shown in figure 40.

REFERENCES

Bandyopadhyay, P. R. & Castano, J. M. 1996 Micro-tiles for electromagnetic turbulence control in saltwater – preliminary investigations. *Symposium on Turbulence Modification and Drag Reduction, ASME Summer Meeting*.

Baron, A. & Quadrio, M. 1996 Turbulent drag reduction by spanwise oscillations. *Appl. Sci. Res.* **55**, 311–326.

Berger, T. W., Kim, J., Lee, C. & Lim, J. 2000 Turbulent boundary layer control utilizing the Lorentz force. *Phys. Fluids* **12**, 631–649.

Bernard, P. S., Thomas, J. M. & Handler, R. A. 1993 Vortex dynamics and the production of Reynolds stress. *J. Fluid Mech.* **253**, 385–419.

Choi, K.-S. 2001 Turbulent drag-reduction mechanisms: Stategies for turbulence management. In *Proc. Turbulence Structure and Modulation* (ed. A. Soldati & R. Monti). Springer.

Choi, K.-S., DeBisschop, J.-R. & Clayton, B. R. 1998 Turbulent boundary layer control by means of spanwise-wall oscillation. *AIAA J.* **36**, 1157–1163.

Chu, D. & Karniadakis, G. E. 1993 The direct numerical simulation of laminar and turbulent flow over riblets. *J. Fluid Mech.* **250**, 1–42.

Crawford, C. H. 1996 Direct numerical simulation of near-wall turbulence: Passive and active control Ph.D. thesis, Princeton University.

Crawford, C. H., Evangelinos, C., Newman, D. & Karniadakis, G. E. 1996 Parallel benchmarks of turbulence in complex geometries. *Computers & Fluids* **25**, 677–698.

Crawford, C. H. & Karniadakis, G. E. 1997 Reynolds stress analysis of EMHD-controlled wall turbulence. Part I. Streamwise forcing. *Phys. Fluids* **9**, 788–806.

Dhanak, M. R. & Si, C. 1999 On reduction of turbulent wall friction through spanwise oscillations. *J. Fluid Mech.* **383**, 175–195.

Donovan, J. F., Kral, L. D. & Cary, A. W. 1997 Characterization of a Lorentz force actuator. *28th AIAA Fluid Dynamics Conference, 4th AIAA Shear Flow Contral Conferences, Snowmass Village, CO, June 29–July 2.*

Du, Y. 1999 Parallel DNS of Electro-Magnetic Flow Control. Ph.D. thesis, Brown University.

Du, Y., Beskok, A. & Karniadakis, G. E. 1999 Simulation of a Lorentz force actuator. In *Proc. 3rd ASME/JSME Joint Fluids Engineering Conference, San Fansisco, CA, 18–22 July.*

Du, Y., Crawford, C. H. & Karniadakis, G. E. 1998 Lorentz force modeling in EMHD turbulence control: DNS studies. In *Proc. Intl Symposium on Seawater Drag Reduction, Newport, RI.*

Du, Y. & Karniadakis, G. E. 2000 Suppressing wall-turbulence via a transverse traveling wave. *Science* **288**, 1230–1234.

Gad-el-Hak, M. 2000 *Flow Control: Passive, Active and Reactive Flow Management*. Cambridge University Press.

Henoch, C. & Stace, J. 1995 Experimental investigation of a salt water turbulent bondary layer modified by an applied streamwise magnetohydrohynamic body force. *Phys. Fluids* **7**, 1371–1383.

Ho, C.-M. 1997 MEMS for aerodynamic control. *AIAA Paper* 97-2118.

Jackson, J. D. 1975 *Classical electrodynamics*. John Wiley & Sons.

Jimenez, J. & Pinelli, A. 1999 The autonomous cycle of near-wall turbulence. *J. Fluid Mech.* **389**, 335–359.

Jung, W. J., Mangiavacchi, N. & Akhavan, R. 1992 Suppression of turbulence in wall-bounded flows by high frequency oscillations. *Phys. Fluids* A **4**, 1605–1607.

Karniadakis, G. E. & Sherwin, S. J. 1999 *Spectral Element/hp Methods for CFD*. Oxford University Press.

Kravchenko, A. G., Choi, H. & Moin, P. 1993 On the relation of near-wall streamwise vortices to wall skin friction in turbulent boundary layers. *Phys. Fluids* **5**, 3307–3309.

Lee, C., Kim, J., Babcock, D. & Goodman, R. 1997 Application of neural networks to turbulence control for drag reduction. *Phys. Fluids* **9**, 1740–1747.

Motz, H. 1946 The treatment of singularities of partial differential equations by relaxation methods. *Q. Appl. Maths* **4**, 371–377.

Nabors, K., Kim, S. & White, J. 1992 Fast capacitance extraction of general three-dimensional structures. *IEEE Trans. on Microwave Theory and Techniques* **40**, 1496–1506.

Near, C. D. 1996 Piezoelectric actuator technology. *SPIE* **2717**, 246–258.

Nieuwstadt, F. T. M. & DenToonder, J. M. J. 2001 Drag reduction by additives: A review. In *Proc. Turbulence Structure and Modulation* (ed. A. Soldati & R. Monti). Springer.

Nosenchuck, D. M. 1996 Boundary layer control using the Lorentz force. In *Proc. ASME Fluid Engng Meeting, San Diego, July 7–11*.

Nosenchuck, D. M. & Brown, G. L. 1993 Discrete spatial control of wall shear stress in a turbulent bondary layer. *Intl Conf. on Near-Wall Turbulent Flows, Tempe Arizona* (ed. C. G. Speziale & B. E. Launder).

O'Sullivan, P. L. & Biringen, S. 1998 Direct numerical simulations of low Reynolds number turbulent channel flow with EMHD control. *Phys. Fluids* **10**, 1169–1181.

Rathnasingham, R. & Breuer, K. S. 1997 System identification and control of a turbulent boundary layer. *Phys. Fluids* **9**, 1867–1869.

Rediniotis, O. K., Lagoudas, D. C. & Wilson, L. N. 2000 Development of a shape-memory alloy actuated biomimetic hydrofoil. *AIAA Paper* 2000-0522.

Schoppa, W. & Hussain, F. 1997 Genesis and dynamics of coherent structures in near-wall turbulence. In *Proc. Self-Sustaining Mechanisms of Wall Turbulence* (ed. R. Panton), p. 385. Computational Mechanics Publications.

Sirovich, L. & Karlsson, S. 1997 Turbulent drag reduction by passive mechanisms. *Nature* **388**, 753–755.

Sureshkumar, R., Beris, A. N. & Handler, R. A. 1997 Direct numerical simulation of the turbulent channel flow of a polymer solution. *Phys. Fluids* **9**, 743–755.

Swearingen, D. & Blackwelder, R. 1987 The growth and breakdown of streamwise vortices in the presence of a wall. *J. Fluid Mech.* **182**, 255–290.

Tiederman, W. G. 1990 The efect of dilute polymer solution on viscous drag and turbulence structure. In *Structure of Turbulence and Drag Reduction*, pp. 187–200. Springer.

Tsinober, A. 1990 MHD flow drag reduction. In *Viscous Drag Reduction in Boundary Layers* (ed. D. L. Bushnell). AIAA.

Waleffe, F. 1997 On a self-sustaining process in shear flows. *Phys. Fluids* **9**, 883–900.